



# Thermodynamic and kinetic assessments in Co–Cr–Mn system using diffusion data

Sri Pragna Pendem<sup>1,\*</sup> , Li Haoge<sup>2</sup>, Nobufumi Ueshima<sup>1</sup>, Katsunari Oikawa<sup>1</sup>, Yuhki Tsukada<sup>3</sup>, and Toshiyuki Koyama<sup>3</sup>

<sup>1</sup> Department of Metallurgy, Graduate School of Engineering, Tohoku University, Aramaki, Aoba-Ku, Sendai 980-8579, Japan

<sup>2</sup> Mitsubishi Materials Corporation, Sanbo Cho, Sakai-Ku, Sakai 590-0906, Japan

<sup>3</sup> Department of Materials Design Innovation Engineering, Graduate School of Engineering, Nagoya University, Furo-Cho, Chikusa-Ku, Nagoya 464-8603, Japan

Received: 1 June 2023

Accepted: 6 September 2023

© The Author(s), 2023

## ABSTRACT

Atomic mobility and thermodynamic assessments of the fcc Co–Cr–Mn system were performed using the ternary diffusion data. Diffusion couples in the Co-rich region of the ternary fcc Co–Cr–Mn system were prepared and annealed at 900, 1050, and 1150 °C. The concentration profiles across the joint interface were measured using an electron probe microstructure analysis technique. The inter-diffusivities were evaluated using the Whittle–Green method, and the atomic mobility parameters of the fcc phase were evaluated via numerical analysis of the diffusional flux. The thermodynamic parameters of the binary fcc Cr–Mn alloy were also determined using the CALPHAD method during the assessment of the mobility parameters in the Co–Cr–Mn system. The atomic mobility and thermodynamic descriptions obtained in this study were used to simulate the ternary concentration profiles. The excellent agreement between the experimental and simulated diffusion data validates the atomic mobility and thermodynamic parameters evaluated in this study.

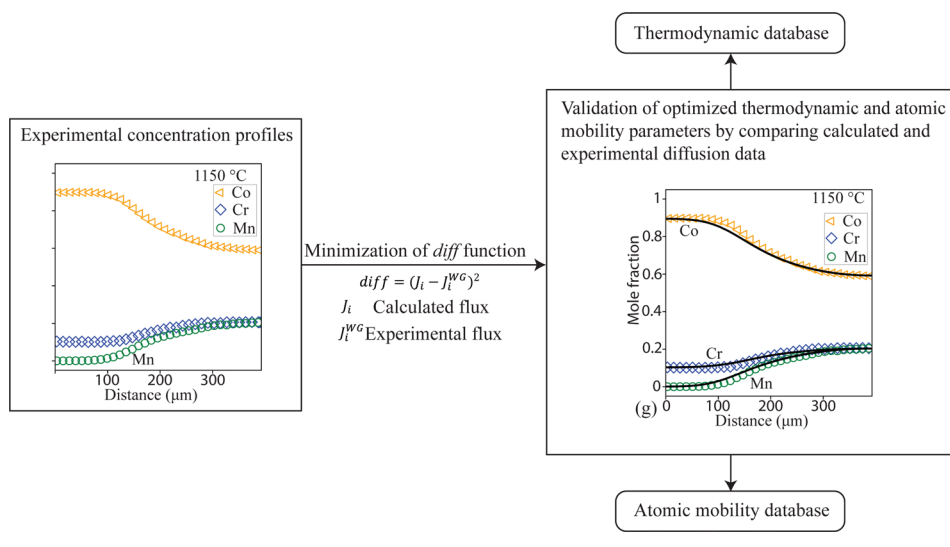
Handling Editor: P. Nash.

Address correspondence to E-mail: sripragna@dc.tohoku.ac.jp

<https://doi.org/10.1007/s10853-023-08927-0>

Published online: 05 October 2023

## GRAPHICAL ABSTRACT



## Introduction

High entropy alloys (HEAs) are defined as alloys with five or more components, and their configurational entropy is larger than  $1.5R$  in their random solution state, here  $R$  is the gas constant [1]. The four core effects of HEAs accommodate its excellent properties: exceptional mechanical strength, high hardness and wear resistance, high-temperature strength, high corrosion, and oxidation resistance [2], and ultrahigh fracture toughness [3]. Recently, several prediction methodologies have been reported to explore new HEAs [4], their phase formations [5], yield strength [6], and elastic properties [7]. Kinetic and thermodynamic databases are the foundational inputs for such predictions when combined with the Calculation of PHase Diagrams (CALPHAD) method [8]. CALPHAD is an established methodology that predicts the properties of multicomponent systems by using the interaction parameters of unary, binary, and ternary systems. The influence of interaction parameters within quaternary or higher-order systems on the CALPHAD method is minimal, primarily attributed to the compounded effect of the multiplication of mole fractions of the constituent elements. Consequently, the evaluation of interaction parameters of ternary or lower-order systems assumes paramount significance in the establishment of a robust thermodynamic database. Kinetic and thermodynamic databases are also important for

modelling diffusion-controlled processes such as precipitation hardening [9], creep rate [10], and phase transformation kinetics [11].

The first step in obtaining the optimized thermodynamic parameters is to obtain numerous experimental data points. The experimental data for thermodynamic assessments usually contain phase equilibrium, and thermochemical and magnetic property data [12]. The second step, optimization, is generally conducted using the CALPHAD method and the least mean square fitting of the experimental data. The user could adjust the initial values of the thermodynamic parameters and error weights to reproduce the experimental information. When the phase equilibrium region is extremely narrow, as in the case of the fcc phase in binary Cr–Mn alloy [12], it is difficult to obtain accurate experimental data and evaluate the optimized thermodynamic parameters. Experimental data of the ternary alloys are conventionally used to compensate for this limitation. This study proposes a method that utilizes the diffusion data of a ternary system to determine the optimized thermodynamic parameters of narrow-phase regions.

In our previous work, the phase equilibria of the ternary Cr–Fe–Mn [13], Co–Cr–Mn [14] and Cr–Mn–Ni [15] subsystems were investigated and the stability regions of the bcc, fcc, and  $\sigma$  phases were clarified. Experimental data could not be obtained for ternary systems containing Mn to construct a diffusion

database for the Cantor alloy. Therefore, atomic mobility assessments by diffusion coupling experiments in the fcc region have been performed for ternary systems containing Mn and have already been reported for the Co–Fe–Mn system [16].

Co–Cr–Mn alloy is a ternary subsystem of the widely known Cantor alloy. The kinetic and thermodynamic descriptions of the Co–Cr–Mn system are crucial for simulating diffusion and phase diagrams of the Cantor alloy using the CALPHAD method. In this study, thermodynamic analysis and atomic mobility assessment were carried out by diffusion couple experiments in the fcc Co–Cr–Mn ternary system to facilitate the simulation of diffusion kinetics, phase stability and microstructural changes in the Cantor alloy using the CALPHAD method.

## Literature review

### Phase diagrams and thermodynamic properties

A detailed review of the phase equilibria and thermodynamic properties of binary Co–Cr, Co–Mn, and Cr–Mn systems are included in Wang et al. [17], our previous research [16], and Lee et al. [12], respectively.

Previous studies on the thermodynamic assessment of binary Co–Cr system can be found in [18–25]. Oikawa et al. [19] assessed the Co–Cr system by considering the thermodynamic properties, magnetic properties, and experimental data. The phase separation between the ferromagnetic and paramagnetic fcc phases in the Co-rich region was studied in [19]. Wang et al. [23] stated that the deviations of calculated  $\sigma$  phase boundaries from the experimental data in [18–22] needed for an accurate thermodynamic model to describe the  $\sigma$  phase. Zhao et al. [24] and Shang et al. [25] used the CALPHAD approach combined with first-principles calculations for thermodynamic assessment in Co–Cr system. Experimental enthalpies of mixing of the solid solutions for the fcc Co–Cr system are consistent with the calculated values [24] from the previous assessments [18, 22]. The thermodynamic parameters from [19, 23] reproduce experimental data well and were employed in this study as they produce a better kinetic assessment. Huang et al. [26] performed a thermodynamic assessment of binary Co–Mn system and is considered in this study.

The phases in binary Cr–Mn include A3, A12, A13, bcc, fcc, hcp, h- $\sigma$  (high- $\sigma$ ), liquid, and  $\sigma$ . Hellawell

and Hume–Rothery [27] and Lugscheider and Etmayer et al. [28] provided experimental information on the narrow fcc region of the Cr–Mn system. In the thermodynamic assessment of the Cr–Mn system [12], experimental information on the fcc/bcc equilibria in the Cr–Fe–Mn ternary system [29] was also considered in the optimization in to reduce errors in temperature and composition measurement in the narrow fcc region. All thermodynamic interaction parameters except for  $L_{CrMn}^{fcc}$  in the Cr–Mn system were adopted from the assessment by Lee et al. [12]. Here,  $L_{CrMn}^{fcc}$  represents the thermodynamic interaction parameter between Cr and Mn in the fcc phase, which was re-evaluated in this study.

Precipitation hardening plays a vital role in tailoring the mechanical properties of the Cantor alloy. Among all the precipitates, the brittle  $\sigma$  phase formed at the grain boundaries of the fcc phase significantly contributes to its high strength [30]. The  $\sigma$  phase in the cantor alloys comprises majority of Cr and some Co, Fe, Mn, and very limited Ni [31]. Hence, experimental information on ternary Co–Cr–Mn phase diagrams has gained much attention recently and is ongoing research. Li, Han, and Kuzovchikov et al. [14, 30, 32] provided experimental information of the ternary Co–Cr–Mn system. A CALPHAD-type thermodynamic assessment was performed [33] based on the available experimental data [14]. Isothermal sections at 900, 1050, and 1150 °C of ternary Co–Cr–Mn phase diagram by Li et al. [14] were considered in this study.

### Atomic mobility assessment

Zhang et al. [34] performed a kinetic assessment of binary Co–Cr alloys by DICTRA software [35, 36], using experimental data from previous studies [37–39]. Good agreement between the calculated [34] and experimental interdiffusion coefficients [37] confirmed the validity of the parameters. Zhang et al. [34] also indicated that the interdiffusivities in fcc Co–Cr binary systems depend considerably on magnetic transitions; thus, the magnetic contribution in the fcc Co–Cr–Mn system was considered in this study. A thorough review of the atomic mobility assessment of binary Co–Mn system was presented in [16]. Considering the limited experimental data in [40], the atomic mobility parameters in binary Co–Mn were reassessed using abundant ternary diffusion data, which were validated by comparing the experimental [40–42] with the calculated diffusion data [16] of the

fcc ternary Co–Fe–Mn and binary Co–Mn systems in [16]. In the Mn-rich region of the Cr–Mn system, the narrow fcc single-phase region and high vapor pressure of Mn make it difficult to experimentally measure the Cr–Mn binary diffusion kinetics in the fcc region, which has not been reported thus far.

Ternary interdiffusivities can be obtained by high-throughput determination of interdiffusion coefficients [43], novel approach for evaluating interdiffusion coefficients [44], pragmatic numerical inverse method [45], pseudo-binary (PB) diffusion couple method [46] and Whittle–Green method [47]. High-throughput determination of interdiffusion coefficients [43], novel approach for evaluating interdiffusion coefficients [44], and pragmatic numerical inverse method [45] minimise the error between measured and calculated composition profiles to determine the optimized mobility interaction parameters. The time taken to solve the minimisation problem using calculated composition profiles of many diffusion couples is considerably huge. In addressing this challenge, our prior work [16] incorporated experimental and calculated flux data at each point across diffusion distance of all diffusion couples. The advantage of using flux over other diffusion data such as interdiffusivities and impurity diffusion coefficients is that flux at each position across diffusion distance can be obtained increasing the dataset available for optimization. Experimental composition profiles and interdiffusivities were compared and found to be in excellent agreement with the calculated ones to validate the optimized mobility interaction parameters. Ternary interdiffusivities from experimental composition profiles can be determined by using PB diffusion couple method [46] and Whittle–Green method [47]. Diffusion of only two constituent elements is developed while maintaining a constant concentration of the third element in PB diffusion couple. However, when the concentration of the third element is held at a constant high, the chemical potential of this element significantly influences the diffusion kinetics within the system. Therefore, in this study, the Whittle–Green method [47] has been adapted for determining the ternary interdiffusivities from experimental data.

## Experimental methodology

Cast ingots weighing approximately 20 g were prepared in an electric arc furnace on a water-cooled copper hearth shielded by an argon atmosphere, using high purity Co (> 99.9 wt. %), Cr (> 99.99 wt. %), and Mn (> 99.9 wt. %). Each alloy was remelted five times to ensure compositional homogeneity. Subsequently, diffusion couples were prepared to determine atomic mobility parameters. Samples with dimensions of 5 mm × 5 mm × 5 mm were cut from the ingots. All surfaces were ground, and one was polished to obtain a mirror finish. Two polished surfaces were placed together, and the well-contacted diffusion couple was fixed using a specially made Mo clamp to form a diffusion-couple assembly, as shown in Fig. 1. It was then placed in a quartz glass capsule backfilled with argon gas for heat treatment. Table 1 lists the composition and annealing time for different diffusion couples quenched in ice water after the heat treatment. The compositions of all the alloys were designed on the Co-rich side, and the temperatures for the heat treatment were selected based on the stable fcc single-phase region on the existing experimental isothermal sections [14]. After quenching, the samples were polished until 2000# and buffed using one  $\mu\text{m}$  diamond spray. The final polishing was conducted via vibration polishing for 12 h using colloidal silica (OP-S Suspension–0.04  $\mu\text{m}$ ). The concentration penetration profiles across the joint interface were investigated using a wavelength dispersive

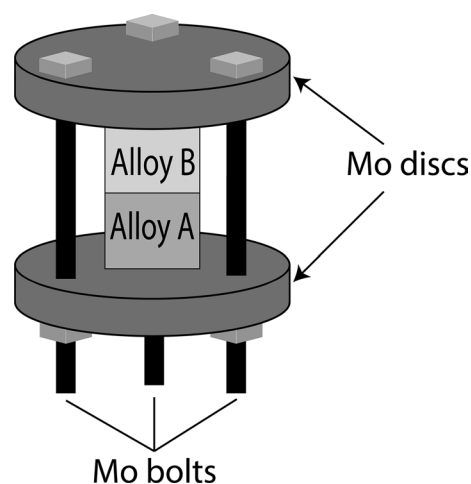


**Figure 1** Schematic diagram showing Mo clamp of diffusion couples.

**Table 1** Terminal compositions and annealing time for the fcc Co–Cr–Mn diffusion couples

Diffusion couple	Mole fraction	Temperature (°C)	Time (hrs)
A1	0.0Cr–0.1Mn/0.1Cr–0.0 Mn	900	240
A2	0.0Cr–0.15Mn/0.1Cr–0.0Mn	900	240
A3	0.2Cr–0.0Mn/0.0Cr–0.15Mn	900	240
A4	0.2Cr–0.0Mn/0.0Cr–0.2Mn	900	240
A5	0.2Cr–0.2Mn/0.0Cr–0.0Mn	900	240
A6	0.1Cr–0.3Mn/0.1Cr–0.2Mn	900	240
A7	0.1Cr–0.4Mn/0.1Cr–0.3Mn	900	240
B1	0.0Cr–0.1Mn/0.1Cr–0.0Mn	1050	144
B2	0.1Cr–0.0Mn/0.0Cr–0.15Mn	1050	144
B3	0.0Cr–0.0Mn/0.1Cr–0.2Mn	1050	144
B4	0.0Cr–0.3Mn/0.2Cr–0.2Mn	1050	144
B5	0.0Cr–0.0Mn/0.1Cr–0.1Mn	1050	144
B6	0.1Cr–0.3Mn/0.1Cr–0.2Mn	1050	144
C1	0.0Cr–0.1Mn/0.1Cr–0.0Mn	1150	96
C2	0.0Cr–0.15Mn/0.1Cr–0.0Mn	1150	96
C3	0.0Cr–0.15Mn/0.2Cr–0.0Mn	1150	96
C4	0.0Cr–0.0Mn/0.1Cr–0.1Mn	1150	96
C5	0.0Cr–0.0Mn/0.2Cr–0.2Mn	1150	96
C6	0.1Cr–0.3Mn/0.1Cr–0.2Mn	1150	96
C7	0.1Cr–0.0Mn/0.2Cr–0.2Mn	1150	96
C8	0.0Cr–0.3Mn/0.1Cr–0.2Mn	1150	96

spectroscopy (WDS) equipped with a field-emission electron probe microanalyzer (FE-EPMA). The accelerating voltage and probe currents were 15 kV and  $2.5 \times 10^{-8}$  A for composition analysis.

### Modelling

This section presents the formulae and theories used for the thermodynamic and kinetic assessments. Thermodynamic and kinetic assessments were performed using an in-house Python code. In a ternary substitutional solid solution with components *A*, *B*, and *C*, the interdiffusion flux ( $J_i$ ) of any component '*i*' ( $i = A, B$ ) is given by Eq. (1), which is Fick's first law for ternary systems [48].

$$J_i = -D_{iA}^C \nabla C_A - D_{iB}^C \nabla C_B \tag{1}$$

where  $D_{iA}^C, D_{iB}^C$  are the interdiffusivities related to the diffusion of element *i* in C matrix caused by concentration gradient of A and B element, respectively.

$D_{AA}^C, D_{BA}^C, D_{AB}^C$  and  $D_{BB}^C$  form a ternary interdiffusion matrix.  $C_{i'}$  and  $\nabla C_{i'}$  represent the mole concentration ( $\frac{\text{mole}}{\text{volume}}$ ) and its gradient of element '*i*', respectively. Assuming that the partial molar volumes are constant, the interdiffusion coefficient depends on thermodynamic and kinetic terms, as shown in Eq. (2).

$$D_{ij}^C = \sum_k (\delta_{ki} - X_i) X_k M_k \left( \frac{\partial \mu_k}{\partial X_j} - \frac{\partial \mu_k}{\partial X_C} \right) + s \left[ (M_k - X_A M_A - X_B M_B - X_C M_C) \frac{2X_i \sum_p X_p M_p \left( \frac{\partial \mu_p}{\partial X_j} - \frac{\partial \mu_p}{\partial X_C} \right)}{A_0 \sum_p X_p M_p} \right] \tag{2}$$

where  $\delta_{ki}$  is the Kronecker delta ( $\delta_{ki} = 1$  if  $k = i$ ; else  $\delta_{ki} = 0$ ), and  $X_i$  is the mole fraction.  $M_k, \mu_k$  are the mobility and chemical potential of element '*k*', respectively.  $A_0$  is a crystal structure dependent pure number and is 7.15 for fcc [49]. The mobility of element '*k*' is expressed as

$$M_k = \frac{1}{RT} \exp\left(\frac{\varphi_k}{RT}\right), \tag{3}$$

where R is the gas constant, and *T* is the temperature. The composition dependence of parameter  $\varphi_k$  can be described by the Redlich–Kister expansion [50], as shown in Eq. (4).

$$\varphi_k = \sum_m X_m \varphi_k^m + \sum_p \sum_{q>p} X_p X_q \sum_{r=0}^n {}^r \varphi_k^{p,q} (X_p - X_q)^r, \tag{4}$$

where  $\varphi_k^m$ , and  ${}^r \varphi_k^{p,q}$  are mobility parameters that are usually linearly related to the temperature. The unknown binary and ternary mobility parameters of the Co–Cr–Mn system were determined in this study.  $\frac{\partial \mu_k}{\partial X_j}$  is the partial derivative of the chemical potential of element '*k*' with respect to the mole fraction of element '*j*', which can be obtained [43] using Gibbs energy as stated in Eq. (5). The second term in Eq. (2) represents the vacancy wind effect. Its consideration depends on the value of '*s*' ( $s = 0$  or  $1$ ). The vacancy wind effect was considered in this study ( $s = 1$ ) to incorporate the total effect of the vacancy wind on the atomic mobility parameters listed in Table 3.

$$\frac{\partial \mu_k}{\partial X_j} = \frac{\partial^2 G_m}{\partial X_k \partial X_j} - \sum_p X_p \frac{\partial^2 G_m}{\partial X_j \partial X_p} \tag{5}$$

Here,  $G_m$  is the total molar Gibbs energy and can be written in terms of contributions from physical and chemical bonding, crystal structure, type of interactions between components, and magnetic characteristics. In phase ‘ $ph$ ,’ the total molar Gibbs free energy is expressed in Eq. (6):

$$G_m^{ph} = {}^0G_m^{ph} - T^0 S_m^{ph} + {}^{Ex}G_m^{ph} + {}^{mag}G_m^{ph}, \tag{6}$$

where  ${}^0G_m^{ph}$  is the molar Gibbs energy of the unreacted pure components in a solid solution, as shown in Eq. (7).

$$G_m^{ph} = \sum_i X_i {}^0G_i, \tag{7}$$

where  ${}^0G_i$  is the standard Gibbs free energy of component ‘ $i$ .’ In the second term of Eq. (6),  ${}^0S_m^{ph}$  is the configurational entropy, which is expressed in terms of the mole fraction, as given in Eq. (8).

$${}^0S_m^{ph} = -R \sum_i X_i \ln X_i, \tag{8}$$

The excess Gibbs energy ( ${}^{Ex}G_m^{ph}$ ) can be expressed as follows

$${}^{Ex}G_m^{ph} = \sum_i \sum_{j>i} X_i X_j \sum_r {}^rL_{ij}(X_i - X_j)^r, \tag{9}$$

where  ${}^rL_{ij}$  is the thermodynamic interaction parameter between elements ‘ $i$ ’ and ‘ $j$ ’.  $L_{CrMn}^{fcc}$  was reassessed in this study while performing the optimization. The fourth term in Eq. (6) is from the magnetic ordering, which was first expressed by Inden [51] and later modified by Hillert and Jarl [52] as

$${}^{mag}G_m^{ph} = RT \ln(\beta + 1) f(\tau), \tag{10}$$

where  $\beta$  is the Bohr magneton number.  $\tau$  is the normalized temperature ( $T/T_c$ ), and  $T_c$  (Curie temperature) for ternary Co–Cr–Mn alloy is given by Eq. (11). The same expansion as that in Eq. (11) is used for  $\beta$ :

$$T_c = {}^0T_{Co}X_{Co} + {}^0T_{Cr}X_{Cr} + {}^0T_{Mn}X_{Mn} + X_{Co}X_{Cr} [{}^0T_{CoCr} + {}^1T_{CoCr}(X_{Co} - X_{Cr})] + X_{Co}X_{Mn} [{}^0T_{CoMn} + {}^1T_{CoMn}(X_{Co} - X_{Mn})], \tag{11}$$

where  ${}^0T_i$  and  ${}^0T_{ij}$  are the magnetic transition temperatures of pure element ‘ $i$ ’ and binary alloy ‘ $ij$ ’, respectively, and we assumed  ${}^rT_{CrMn}$  to be zero.  $f(\tau)$  is expressed by Eqs. (12) and (13) when  $\tau < 1$  and  $\tau > 1$ , respectively:

$$f(\tau) = 1 - \frac{\left[ \frac{79\tau^{-1}}{140p} + \frac{474}{497} \left( \frac{1}{p} - 1 \right) \left( \frac{\tau^3}{6} + \frac{\tau^9}{135} + \frac{\tau^{15}}{600} \right) \right]}{A}, \tag{12}$$

$$f(\tau) = -\frac{\left( \frac{\tau^{-5}}{10} + \frac{\tau^{-15}}{315} + \frac{\tau^{-25}}{1500} \right)}{A}, \tag{13}$$

where  $A$  is given by  $A = \frac{518}{1125} + \frac{11692}{15975} \left( \frac{1}{p} - 1 \right)$ .  $p$  is a constant dependent on the crystal structure and is 0.28 for the fcc structure. In addition to Onsager’s formula, Eq. (1), the flux at each point of the composition profile can be obtained using the Whittle–Green method [47], as shown in Eq. (14):

$$J_i^{WG} = \frac{1}{2t} (C_i^+ - C_i^-) \left[ (1 - Y_i) \int_{-\infty}^x Y_i dx + Y_i \int_x^{+\infty} (1 - Y_i) dx \right], \tag{14}$$

where  $J_i^{WG}$  is the flux obtained from the experimental data and Whittle–Green method.  $t$  is the annealing time and  $Y_i$  is given by  $Y_i = \frac{C_i - C_i^-}{C_i^+ - C_i^-}$ . Here,  $C_i^-$  and  $C_i^+$  are the mole concentrations of element ‘ $i$ ’ on the left and right ends of the diffusion couple, respectively. The squared difference between the experimental and calculated fluxes given by  $diff = (J_i - J_i^{WG})^2$  at each point of the composition profile, was calculated, and the summation was minimized for kinetic and thermodynamic assessments. Here,  $diff$  is a function to be minimized to obtain the optimized parameters. All function minimizations in this study were performed using the SciPy library [53] and the Nelder–Mead optimization technique [54]. After establishing and validating the values of the thermodynamic interaction parameters by comparing the calculated phase diagram with the existing experimental data, the optimized  $L_{CrMn}^{fcc}$  was used to determine the accurate values of the mobility parameters. This procedure was repeated until all the parameters were optimized. Figure 2 shows the schematic diagram of the flow of optimization process. Reasons for choosing experimental and calculated flux to solve the minimization problem are mentioned in Sect. “Atomic mobility assessment”. In instances involving simple functions wherein the attainment of the global minimum is feasible without

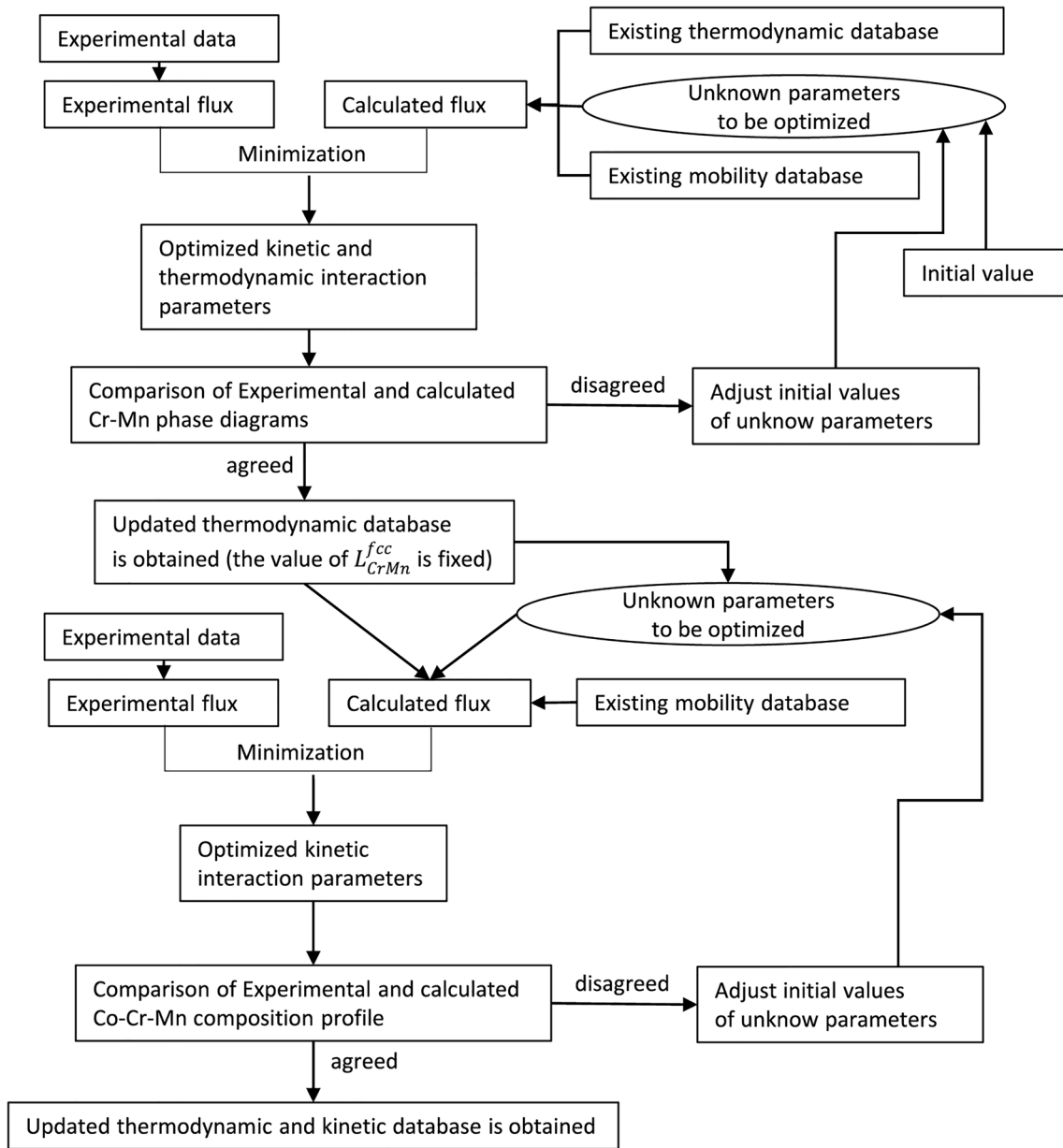


**Figure 2** Schematic diagram of the flow of optimization to determine the atomic mobility and thermodynamic interaction parameters.

encountering entrapment within local minima, the selection of initial values becomes inconsequential. For multi variable functions, it may become necessary to repetitively experiment with a range of initial parameters as shown in Fig. 2 to confirm the achievement of the global minimum solution. Fixing  $L_{CrMn}^{fcc}$  ensured obtaining reasonable values of mobility interaction parameters that improve the agreement between calculated and experimental concentration profiles.

Ternary interdiffusivity matrices [ $D_{CrCr}^{Co}$ ,  $D_{CrMn}^{Co}$ ,  $D_{MnMn}^{Co}$ , and  $D_{MnCr}^{Co}$ ] at the intersection points of the composition profiles at 900, 1050, and 1150 °C were also determined using the Whittle–Green method, as given in the following equations.

$$\frac{1}{2t} \left( \frac{dx}{dY_{Cr}} \right) \left[ (1 - Y_{Cr}) \int_{-\infty}^x Y_{Cr} dx + Y_{Cr} \int_x^{+\infty} (1 - Y_{Cr}) dx \right] = D_{CrCr}^{Co} + D_{CrMn}^{Co} \frac{dC_{Mn}}{dC_{Cr}}, \quad (15)$$

$$\frac{1}{2t} \left( \frac{dx}{dY_{Mn}} \right) \left[ (1 - Y_{Mn}) \int_{-\infty}^x Y_{Mn} dx + Y_{Mn} \int_x^{+\infty} (1 - Y_{Mn}) dx \right] = D_{MnMn}^{Co} + D_{MnCr}^{Co} \frac{dC_{Cr}}{dC_{Mn}}, \quad (16)$$

interdiffusivities  $D_{CrCr}^{Co}$ ,  $D_{CrMn}^{Co}$ ,  $D_{MnMn}^{Co}$ , and  $D_{MnCr}^{Co}$  can be evaluated. The interdiffusivities must conform to the thermodynamic constraints in Eqs. (17–19), as proposed by Kirkaldy et al. [55].

By solving Eqs. (15–16) for two diffusion couples with intersecting composition profiles, four ternary

$$D_{CrCr}^{Co} + D_{MnMn}^{Co} > 0, \quad (17)$$

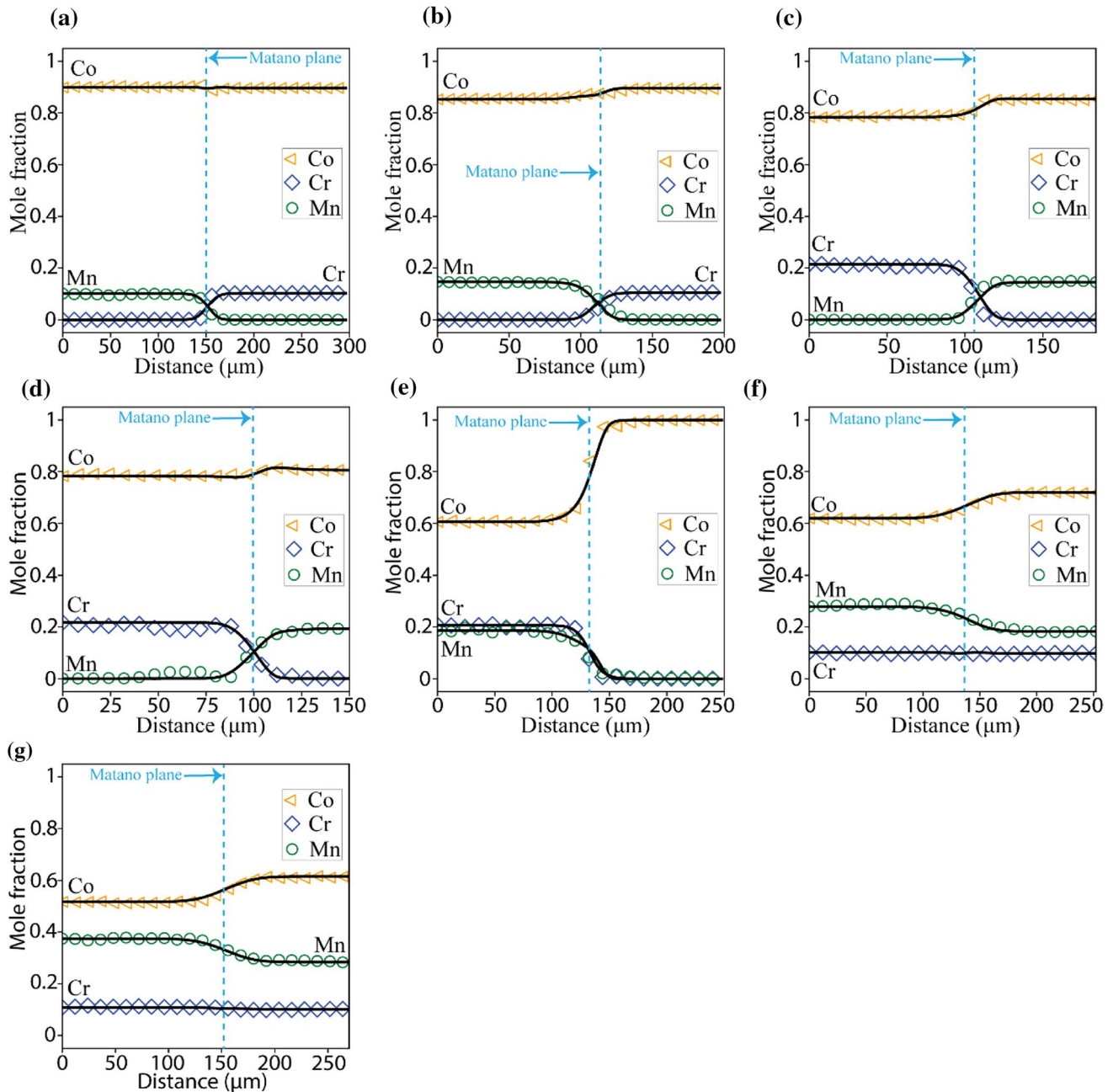


**Figure 3** Comparison of experimental (scatter plot) and calculated (solid lines) composition profiles of diffusion couples **a** A1, **b** A2, **c** A3, **d** A4, **e** A5, **f** A6, and **g** A7 annealed at 900 °C for 240 h.

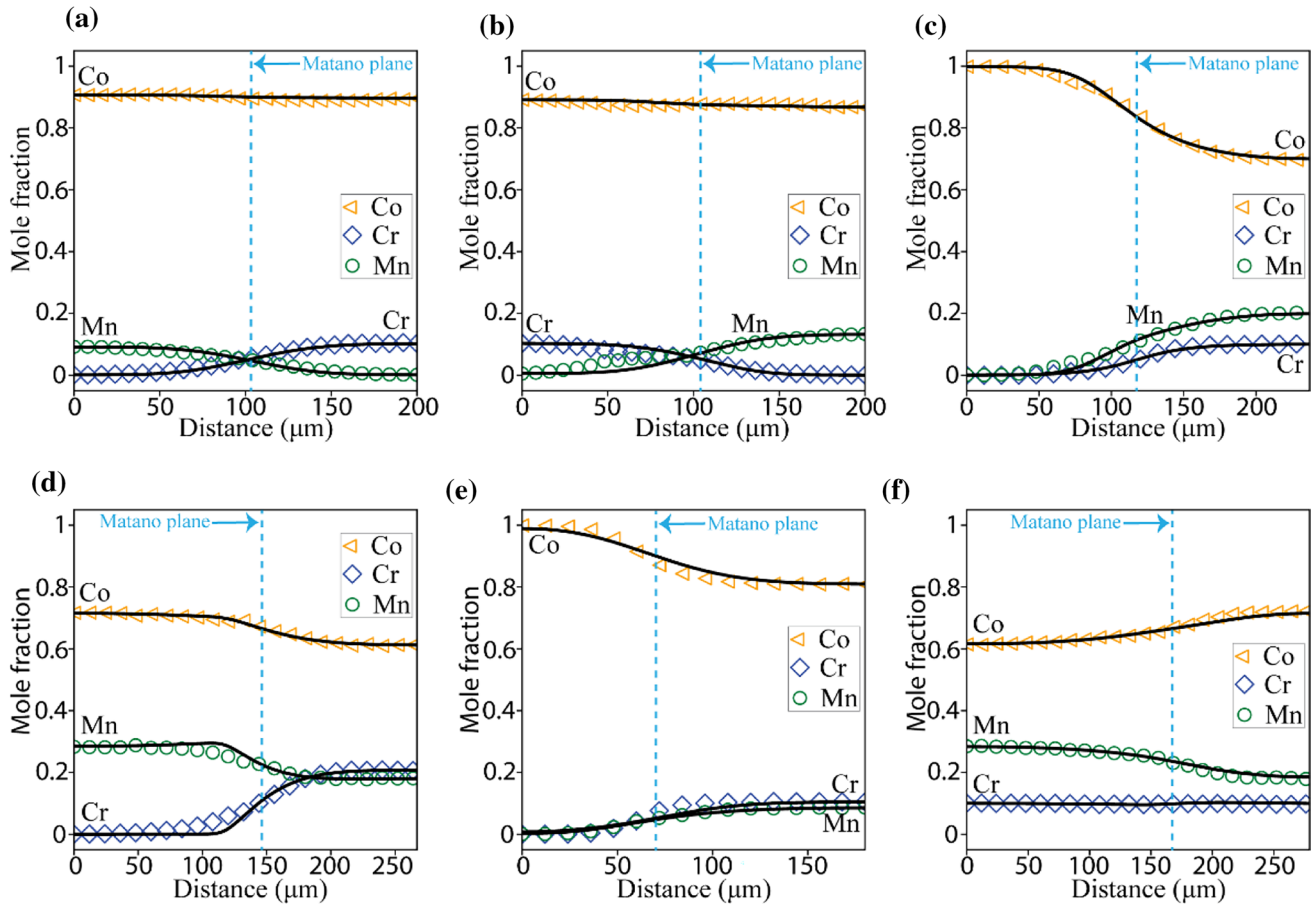


**Figure 4** Comparison of experimental (scatter plot) and calculated (solid lines) composition profiles of diffusion couples **a** B1, **b** B2, **c** B3, **d** B4, **e** B5, and **f** B6 annealed at 1050 °C for 144 h.

$$D_{CrCr}^{Co} D_{MnMn}^{Co} - D_{CrMn}^{Co} D_{MnCr}^{Co} \geq 0, \tag{18}$$

$$(D_{CrCr}^{Co} - D_{MnMn}^{Co})^2 - 4D_{CrMn}^{Co} D_{MnCr}^{Co} \geq 0, \tag{19}$$

where  $C(x)$  is the fitted composition profile as a function of diffusion distance ' $x$ '.  $A_1$ ,  $A_2$ ,  $x_0$ , and  $b_0$  are the fitting parameters and  $x_0$  signifies the position of the Matano plane.

### Results and discussion

After heat treatments, the composition-penetration profiles across the joint interface were measured using EPMA, as shown in Figs. 3, 4, 5. The experimentally observed concentration profiles of Co, Cr, and Mn were symmetric, and a Boltzmann fitting function was used to smoothen the profiles [56], as given by Eq. (20).

$$C(x) = \frac{A_1 - A_2}{1 + e^{\frac{x-x_0}{b_0}}} + A_2, \tag{20}$$

### Thermodynamic re-assessment of fcc Cr–Mn

The thermodynamic parameters of pure fcc Co, Cr, and Mn were obtained from Scientific Group Thermo-data Europe (SGTE) data for pure elements [57]. The magnetic parameters of pure fcc Co [58], Cr [59], Mn [60], binary Co–Cr [19], and Co–Mn [26] were used in this study to calculate the magnetic contribution.

The thermodynamic parameters for the fcc Cr–Mn system were optimized together with the diffusion parameters obtained from the diffusion couple experiments. The optimized thermodynamic

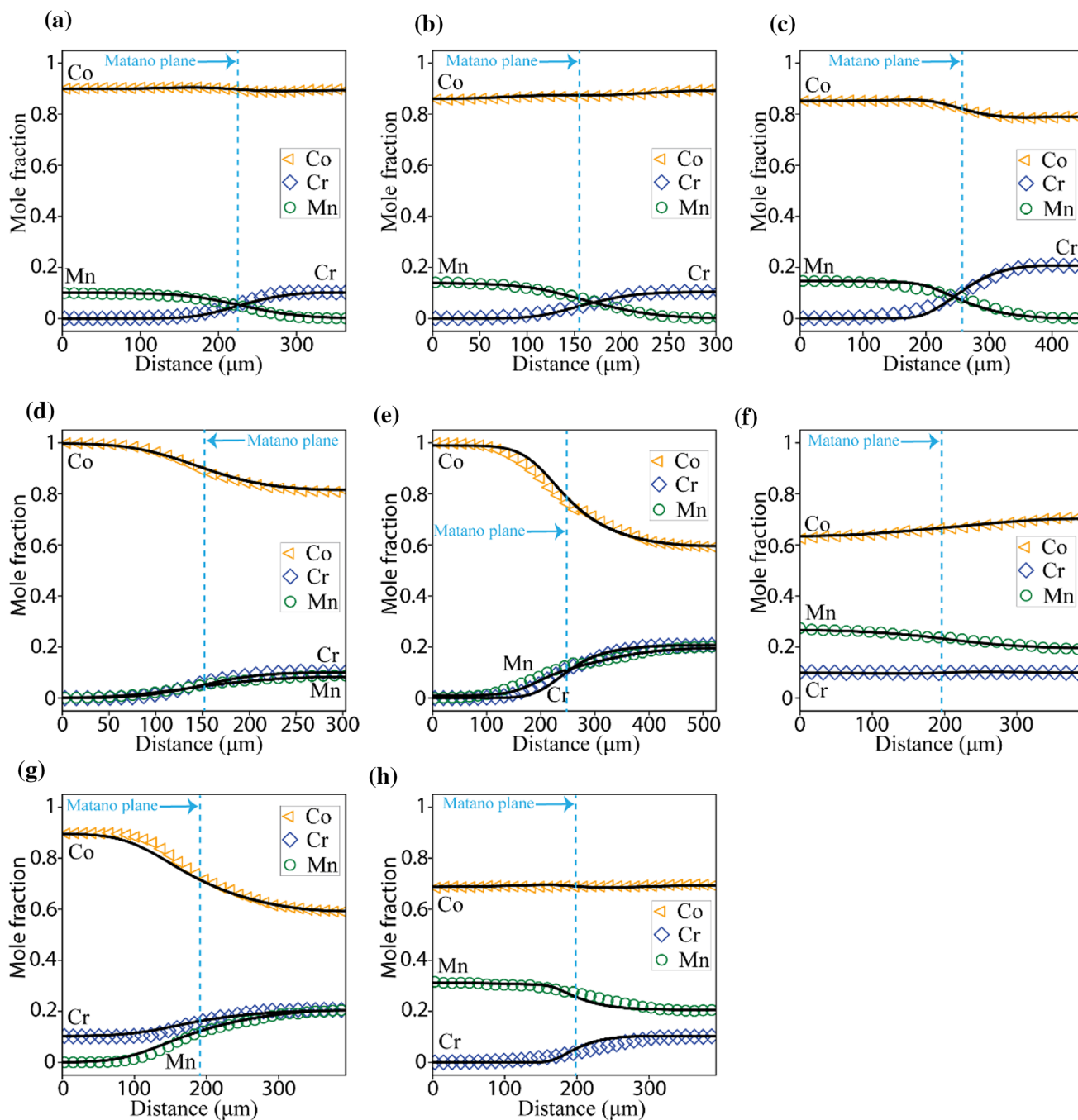


**Figure 5** Comparison of experimental (scatter plot) and calculated (solid lines) composition profiles of diffusion couples **a** C1, **b** C2, **c** C3, **d** C4, **e** C5, **f** C6, **g** C7, and **h** C8 annealed at 1150 °C for 96 h.

parameters are listed in Table 2 and in the supplemental thermodynamic database file; for the A3, A12, A13, bcc, hcp, h- $\sigma$ , liquid, and  $\sigma$  phases of the binary Cr–Mn alloy were adopted from [12]. Atomic mobility assessment was performed using the existing thermodynamic parameters, and calculated concentration profiles (dotted line) are compared with

the experimental data in Fig. 7. Calculated profiles (dotted line) of diffusion couples A3, A4, A5, B3, C3, C5, and C7 deviate considerably from experimental data. Therefore, it is important to optimize Cr–Mn thermodynamic parameters along with atomic mobility parameters in Co–Cr–Mn system to improve the quality of property database. The

**Table 2** Optimized thermodynamic parameters in fcc Co–Cr–Mn system

Parameters (All quantities in SI units)	Reference
$L_{CoCr}^{fcc} = -2256.2 - 7.3908T - 3578.5(X_{Co} - X_{Cr})$	[23]
$L_{CoMn}^{fcc} = -23756 - 2343(X_{Co} - X_{Mn})$	[26]
$L_{CrMn}^{fcc} = -12763.8 + 10.6T - 337.6(X_{Cr} - X_{Mn})$	This work
$T_C^{fcc} = 1396X_{Co} - 1109X_{Cr} - 1620X_{Mn} + X_{Co}X_{Cr}(-9392.5259 + 8383.0424(X_{Co} - X_{Cr})) + X_{Co}X_{Mn}(-2685 + 3657(X_{Co} - X_{Mn}))$	[19, 26]
$\beta_{fcc} = 1.35X_{Co} - 2.46X_{Cr} - 1.86X_{Mn} - 1.07X_{Co}X_{Mn}$	[19, 26]

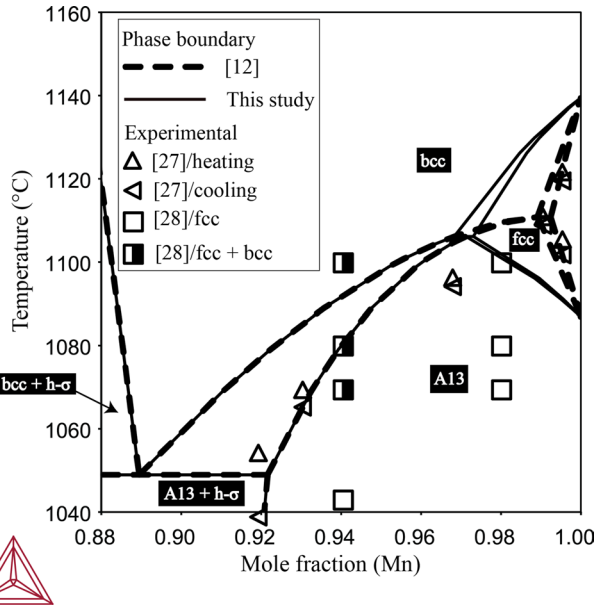


**Figure 6** The phase diagram of binary Cr–Mn system obtained using optimized thermodynamic parameters.

interdiffusion coefficients in multicomponent systems depend on the mobility and thermodynamics (interactions between atoms) of the components, as can be theoretically observed from Eq. (2). This dependence of the flux on interdiffusivity, which further depends on the chemical potentials of the components, was used to compute  $L_{CrMn}^{fcc}$  in this study. A comparison between the experimental phase equilibria data and the calculated Cr–Mn binary phase diagrams obtained by previous [12] and the present assessments using the Thermo-Calc software is shown in Fig. 6. The fcc single-phase region observed in this study is wider than that reported by Lee et. al’s [12] analysis, but is consistent with the previous experimental data. There is a stable fcc phase extending up to 0.973 mol fraction of Mn, which is between 0.93 [28] and 0.99 [27] mole fraction of Mn, as previously determined

**Table 3** Values of optimized mobility parameters in fcc Co–Cr–Mn ternary system

Mobility parameter	Value (J/mol)	Reference
<i>Parameter of Co</i>		
$\phi_{Co}^{Co}$	$-302,004 - 69.02 T$	[61]
$\phi_{Co}^{Cr}$	$-235,000 - 82.00 T$	[64]
$\phi_{Co}^{Mn}$	$-214,997.00 - 82.0 T$	[65]
${}^0\phi_{Co}^{CoCr}$	$-39,154.49$	[34]
${}^0\phi_{Co}^{CoMn}$	$-24,350.71 - 11.84 T$	[16]
${}^1\phi_{Co}^{CoMn}$	$+259,007.11$	[16]
${}^0\phi_{Co}^{CrMn}$	$-30,991.91 + 30.00 T$	This work
${}^1\phi_{Co}^{CrMn}$	$+74,721.70$	This work
<i>Parameter of Cr</i>		
$\phi_{Cr}^{Cr}$	$-235,000 - 82.00 T$	[62]
$\phi_{Cr}^{Co}$	$-253,700 - 97.17 T$	[61]
$\phi_{Cr}^{Mn}$	$-214,997.00 - 82.0 T$	[65]
${}^0\phi_{Cr}^{CoCr}$	$-50,243.34$	[34]
${}^0\phi_{Cr}^{CoMn}$	$-173,670.93 - 63.71 T$	This work
${}^1\phi_{Cr}^{CoMn}$	$+149,190.47$	This work
${}^0\phi_{Cr}^{CrMn}$	$+65,419.99 + 24.06 T$	This work
${}^1\phi_{Cr}^{CrMn}$	$-105,390.7$	This work
<i>Parameter of Mn</i>		
$\phi_{Mn}^{Mn}$	$-212,755.85 - 98.07 T$	[63]
$\phi_{Mn}^{Co}$	$-285,377 - 73 T$	[61]
$\phi_{Mn}^{Cr}$	$-275,000 - 73 T$	[61]
${}^0\phi_{Mn}^{CoCr}$	$+46,149.25 - 8.05 T$	This work
${}^1\phi_{Mn}^{CoCr}$	$-50,835.19$	This work
${}^0\phi_{Mn}^{CoMn}$	$+170,366.89 - 191.2 T$	[16]
${}^1\phi_{Mn}^{CoMn}$	$+73,511.21$	[16]
${}^0\phi_{Mn}^{CrMn}$	$+117,696.07 - 15.61 T$	This work
${}^1\phi_{Mn}^{CrMn}$	$+53,167.67$	This work

experimentally. Stable bcc + fcc and A13 + fcc phases were proposed by Lugscheider and Ettmayer et al. [28], and the bcc + A13 phase, was suggested by Hellowell and Hume–Rothery et al. [27]. Peritectoid

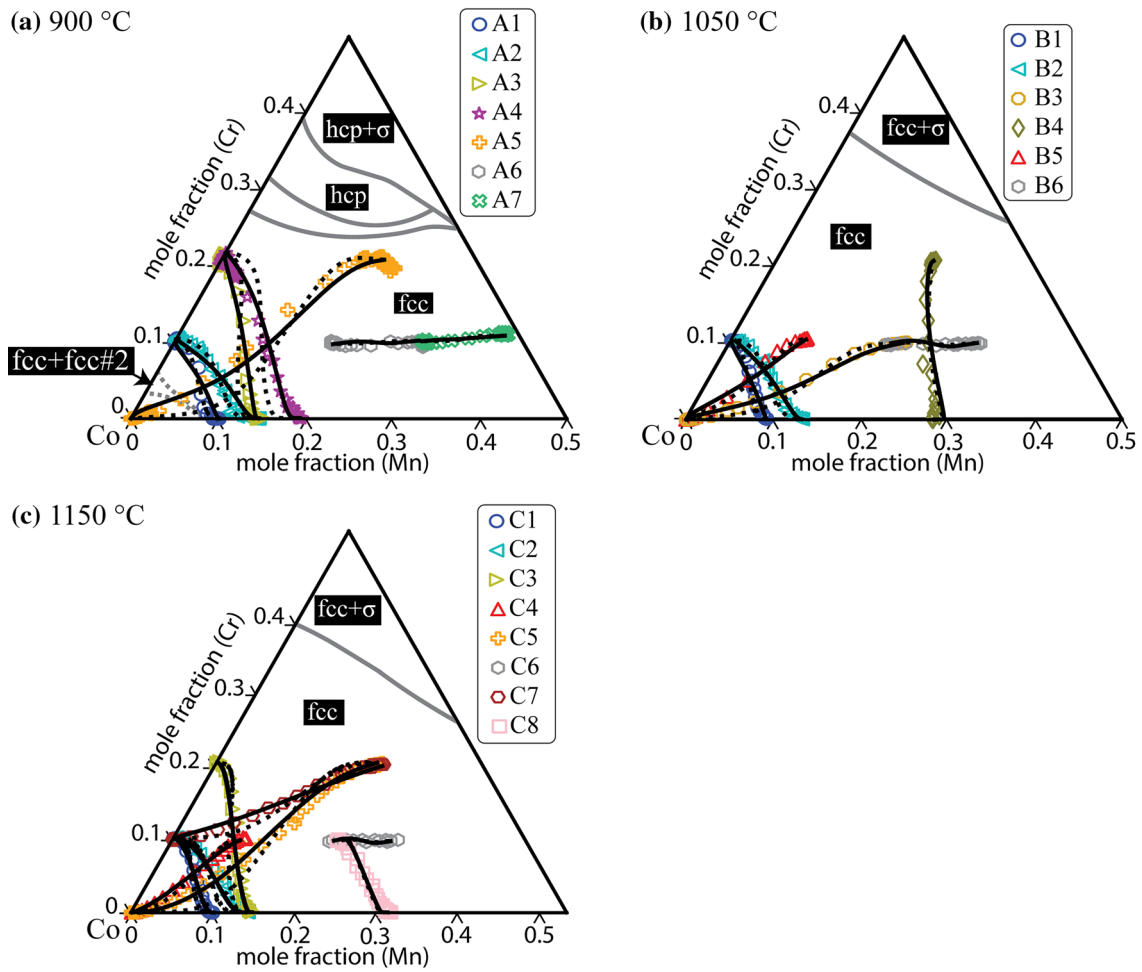


**Figure 7** Comparison of experimental data (scatter plot) and calculated composition profiles using optimized thermodynamic parameters of this study (solid line) and from [12] (dotted line) at

**a** 900 °C, **b** 1050 °C, and **c** 1150 °C on respective isothermal sections of ternary Co–Cr–Mn phase diagram.

**Table 4** Values of ternary interdiffusivities in fcc Co–Cr–Mn system

Temperature (°C)	Composition (at%)	Interdiffusivity ( $m^2/s$ )			
		$D_{CrCr}^{Co}$	$D_{CrMn}^{Co}$	$D_{MnMn}^{Co}$	$D_{MnCr}^{Co}$
900	Co–3.4 Cr–6.7 Mn	$1.45 \times 10^{-17}$	$0.95 \times 10^{-17}$	$6.42 \times 10^{-17}$	$0.61 \times 10^{-17}$
	Co–5.7 Cr–6.4 Mn	$3.05 \times 10^{-17}$	$-0.56 \times 10^{-17}$	$7.19 \times 10^{-17}$	$-0.19 \times 10^{-17}$
	Co–8.8 Cr–8.7 Mn	$1.56 \times 10^{-17}$	$1.07 \times 10^{-17}$	$4.62 \times 10^{-17}$	$1.96 \times 10^{-17}$
	Co–10.9 Cr–9.4 Mn	$2.09 \times 10^{-17}$	$-0.15 \times 10^{-17}$	$4.72 \times 10^{-17}$	$1.91 \times 10^{-17}$
1050	Co–5.0 Cr–5.3 Mn	$0.31 \times 10^{-15}$	$-1.33 \times 10^{-15}$	$1.63 \times 10^{-15}$	$-0.03 \times 10^{-15}$
	Co–5.4 Cr–7.2 Mn	$1.26 \times 10^{-15}$	$-0.47 \times 10^{-15}$	$1.72 \times 10^{-15}$	$0.84 \times 10^{-15}$
	Co–7.6 Cr–5.2 Mn	$0.41 \times 10^{-15}$	$-2.47 \times 10^{-15}$	$4.15 \times 10^{-15}$	$-0.18 \times 10^{-15}$
	Co–9.8 Cr–24.1 Mn	$1.31 \times 10^{-15}$	$0.00 \times 10^{-15}$	$2.27 \times 10^{-15}$	$0.82 \times 10^{-15}$
1150	Co–4.3 Cr–4.7 Mn	$1.71 \times 10^{-15}$	$-1.17 \times 10^{-15}$	$2.80 \times 10^{-15}$	$-0.15 \times 10^{-15}$
	Co–5.0 Cr–7.5 Mn	$3.88 \times 10^{-15}$	$0.57 \times 10^{-15}$	$6.58 \times 10^{-15}$	$2.04 \times 10^{-15}$
	Co–7.0 Cr–5.9 Mn	$1.78 \times 10^{-15}$	$-1.30 \times 10^{-15}$	$4.08 \times 10^{-15}$	$-0.80 \times 10^{-15}$
	Co–7.8 Cr–9.2 Mn	$3.49 \times 10^{-15}$	$1.36 \times 10^{-15}$	$7.22 \times 10^{-15}$	$1.93 \times 10^{-15}$
	Co–14.7 Cr–5.2 Mn	$3.28 \times 10^{-15}$	$0.77 \times 10^{-15}$	$6.17 \times 10^{-15}$	$1.88 \times 10^{-15}$

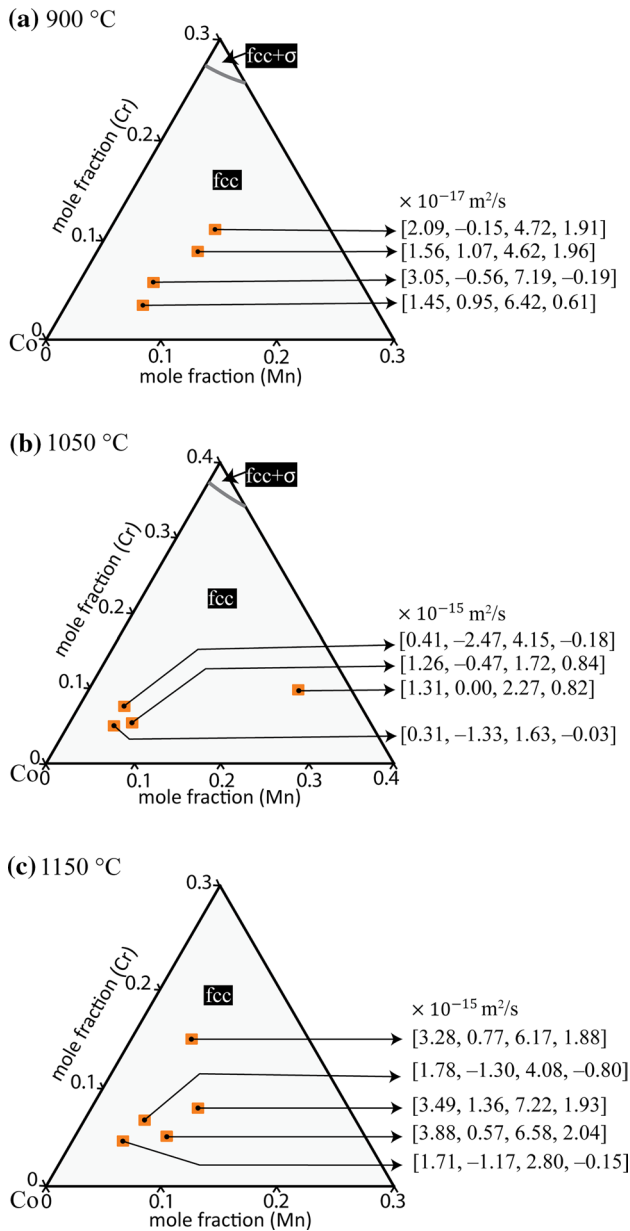


**Figure 8** Ternary interdiffusivities [ $D_{CrCr}^{Co}$ ,  $D_{CrMn}^{Co}$ ,  $D_{MnMn}^{Co}$ , and  $D_{MnCr}^{Co}$ ] obtained using the Whittle–Green method at the intersection points of the composition profiles and at **a** 900 °C, **b** 1050 °C, and **c** 1150 °C are marked on the respective isothermal sections of Co–Cr–Mn system.

(bcc + fcc → A13) and eutectoid reactions (bcc → σ + A13) occur around 97 and 89 at% Mn. The only available experimental data of the bcc/fcc and fcc/A13 phase transformations in Cr–Mn system are from 1950 to 1970s. The experimental data from [27] is approximate only, and the data from [28] is difficult to reproduce by reasonable values of  $L_{CrMn}^{fcc}$  [12].

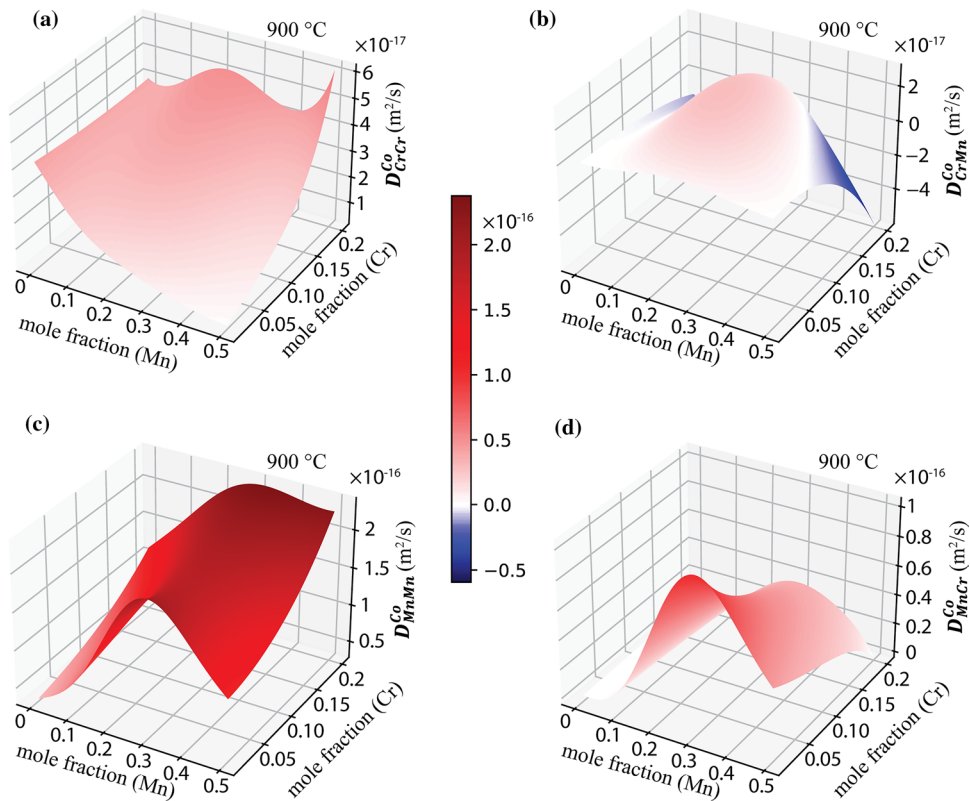
Given the constraints imposed by the limited reliability and reproducibility of the available experimental data, the resultant calculated phase diagram is deemed to be acceptable. Thus, the approach of utilizing diffusion data to determine the thermodynamic interaction parameters can be effectively employed to narrow equilibrium regions where optimization through experimental data is difficult.

### Atomic mobility parameters

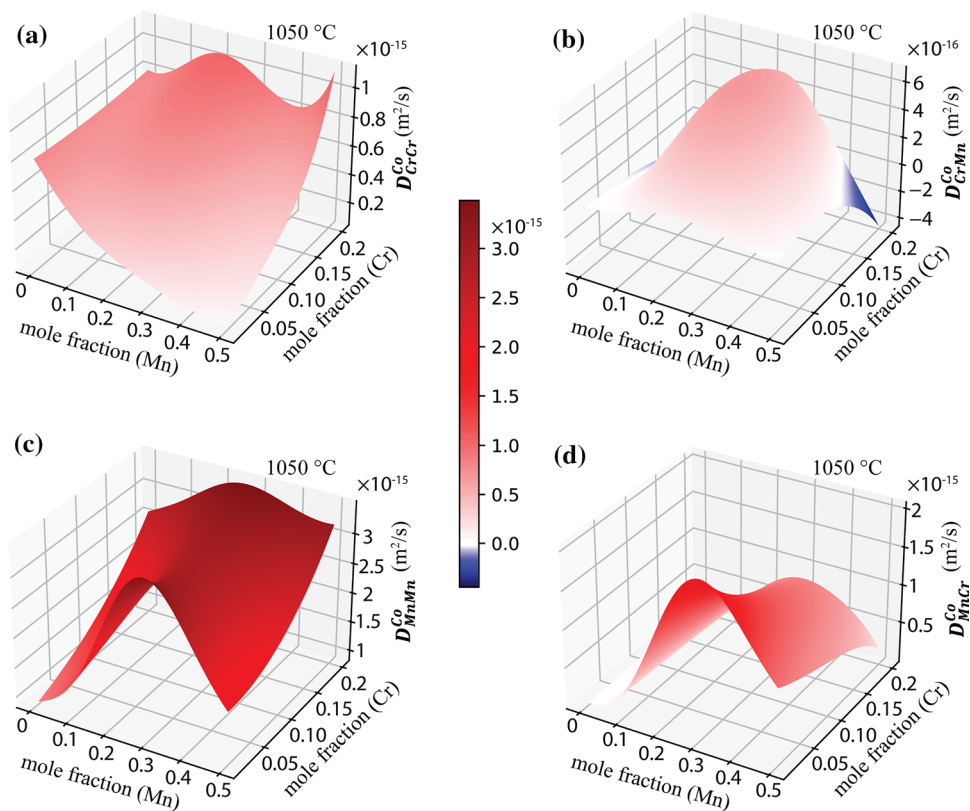
The self-atomic mobility parameters of Co, Cr, and Mn were adopted from Khorasgani [61], Engström [62], and Liu et al. [63], respectively. The impurity mobility parameters of Co in fcc Cr [64], Co in fcc Mn [65], Cr in fcc Co [61], Cr in fcc Mn [65], Mn in fcc Co [61], and Mn in fcc Cr [61] were considered for optimization. The optimized mobility parameters listed in Table 3 and in supplemental mobility database file were determined by minimizing *diff* and using the optimized  $L_{CrMn}^{fcc}$ . The atomic mobility interaction parameters of the fcc Cr–Mn ( $\varphi_{Cr}^{CrMn}$ ,  $\varphi_{Mn}^{CrMn}$ ) binary system and the ternary Co–Cr–Mn ( $\varphi_{Co}^{CrMn}$ ,  $\varphi_{Cr}^{CoMn}$ , and  $\varphi_{Mn}^{CoCr}$ ) were determined (Table 3). The optimized mobility parameters were validated by comparing the experimental and calculated composition profiles (black solid lines) at 900, 1050, and 1150 °C as shown in Figs. 3, 4, 5.

Figure 7 compares the calculated diffusion pathways with the experimental data on the isothermal cross-sections of the Co–Cr–Mn phase diagram [14]. The excellent agreement between the calculated and experimental profiles proves the reliability of the optimized mobility parameters determined in this study. Ternary interdiffusivities were obtained using the Whittle–Green method at the intersection points of the composition profiles, as shown in Table 4 and Fig. 8. The four values at each point in Fig. 8 indicate [ $D_{CrCr}^{Co}$ ,  $D_{CrMn}^{Co}$ ,  $D_{MnMn}^{Co}$ , and  $D_{MnCr}^{Co}$ ], respectively. All interdiffusivities satisfied the three thermodynamic constraints proposed by Kirkaldy et al. [55], and shown in Eqs. 17–19. The values of the main interdiffusivities,  $D_{CrCr}^{Co}$  and  $D_{MnMn}^{Co}$  are all positive, and those of  $D_{MnMn}^{Co}$  were higher than those of  $D_{CrCr}^{Co}$  indicating that the diffusivity of Mn was higher than that of Cr in the fcc ternary Co–Cr–Mn system. The cross interdiffusivities,  $D_{CrMn}^{Co}$  and  $D_{MnCr}^{Co}$  are both negative and positive, signifying negative and positive gradients of the diffusion potential, respectively [66]. The negative values of the cross interdiffusivities  $D_{CrMn}^{Co}$

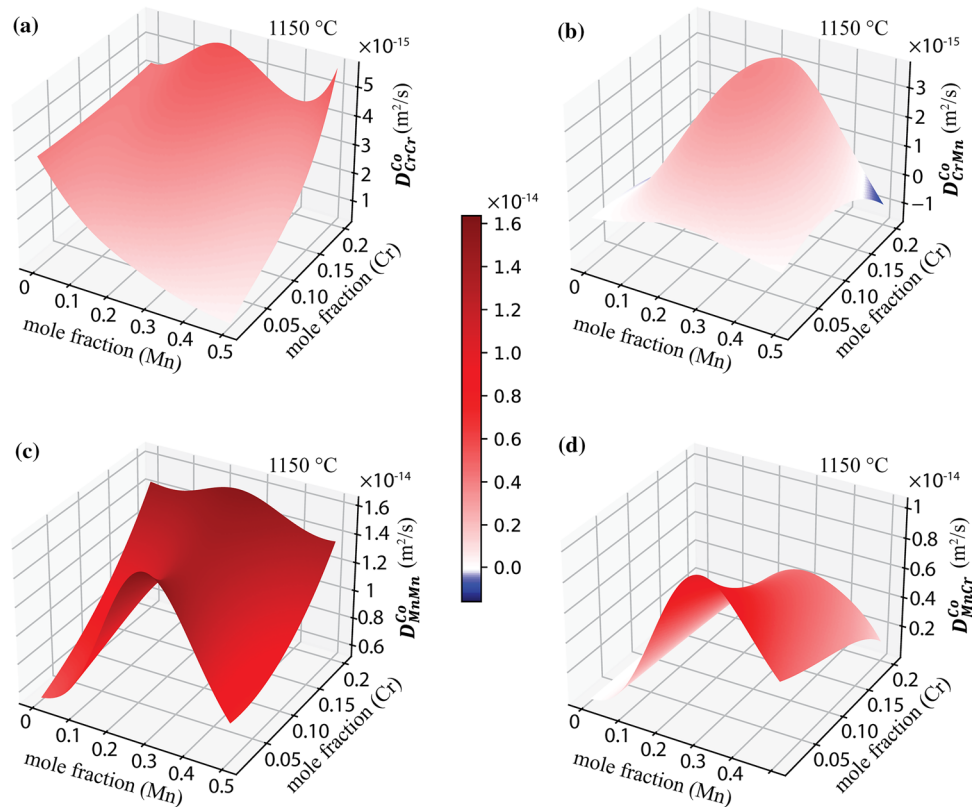
**Figure 9** Surface profiles of calculated composition dependent **a**  $D_{CrCr}^{Co}$ , **b**  $D_{CrMn}^{Co}$ , **c**  $D_{MnMn}^{Co}$ , and **d**  $D_{MnCr}^{Co}$  at 900 °C. Calculated ternary interdiffusivity values are listed in a supplemental data file.



**Figure 10** Surface profiles of calculated composition dependent **a**  $D_{CrCr}^{Co}$ , **b**  $D_{CrMn}^{Co}$ , **c**  $D_{MnMn}^{Co}$ , and **d**  $D_{MnCr}^{Co}$  at 1050 °C. Calculated ternary interdiffusivity values are listed in a supplemental data file.



**Figure 11** Surface profiles of calculated composition dependent **a**  $D_{CrCr}^{Co}$ , **b**  $D_{CrMn}^{Co}$ , **c**  $D_{MnMn}^{Co}$ , and **d**  $D_{MnCr}^{Co}$  at 1150 °C. Calculated ternary interdiffusivity values are listed in a supplemental data file.



and  $D_{MnCr}^{Co}$  suggest that Mn and Cr hinder the diffusion of Cr and Mn, respectively. Figures 9, 10, 11 show the three-dimensional surfaces of calculated  $D_{CrCr}^{Co}$ ,  $D_{CrMn}^{Co}$ ,  $D_{MnMn}^{Co}$ , and  $D_{MnCr}^{Co}$  at 900, 1050, and 1150 °C respectively to observe how interdiffusivities evolve with concentration. The comparison of experimental data with the calculated interdiffusivities is discussed in a supplemental file. All the values of calculated ternary interdiffusivities at 900, 1050, and 1150 °C are satisfying the thermodynamic conditions proposed by Kirkaldy et al. [55], and are listed in a supplemental datafile. Negative values are highlighted in blue and positive values are highlighted in red. All the calculated interdiffusivities increased with temperature. Both the calculated main interdiffusivities,  $D_{CrCr}^{Co}$  and  $D_{MnMn}^{Co}$  increased with the Cr concentration, as shown in Figs. 9, 10, 11. The surface plots of the mobilities of Co, Cr, and Mn in the composition range of interest in this study are shown in Fig. 12. At low Cr content,  $D_{MnMn}^{Co}$  and the mobility of Mn are observed to increase and then decrease with an increase in Mn concentration, indicating that interdiffusivities and mobilities cannot be estimated by simple extrapolation. Equation 2 demonstrates

the dependency of interdiffusivities on mobilities and chemical potentials gradients of Co, Cr, and Mn.  $M_i$  further depends on  $\varphi_i$  which comprises the effect of mobility interaction parameters as shown in Eqs. 3 and 4. To understand the effect of thermodynamic quantities on interdiffusivities, surface plots of chemical potentials of Co, Cr, and Mn at 900, 1050, and 1150 °C are shown in Fig. 13. Chemical potential can be easily calculated from the thermodynamic data of the system [43]. Figure 14 shows the distribution of  $\varphi_{Co}$ ,  $\varphi_{Cr}$ , and  $\varphi_{Mn}$  at 900, 1050, and 1150 °C to assess the dependency of diffusivities and mobilities on mobility interactions between atoms. The Figs. 9, 10, 11 reveal a noteworthy trend: at lower Mn content,  $D_{CrCr}^{Co}$  exhibits relatively minimal variation as Cr content increases. However, in contrast, when the Mn content is high,  $D_{CrCr}^{Co}$  undergoes a substantial increase with increase in Cr content. In regions with low Mn content or, high Co content,  $D_{CrCr}^{Co}$  is influenced by  $\varphi_{Co}$  and  $\mu_{Co}$ . As shown in Figs. 13 and 14, both  $\varphi_{Co}$  and  $\mu_{Co}$  maintain constancy even as the Cr content increases. Hence, at low Mn content,  $D_{CrCr}^{Co}$  is governed by both mobility and thermodynamic interactions. In the high Mn content region, the

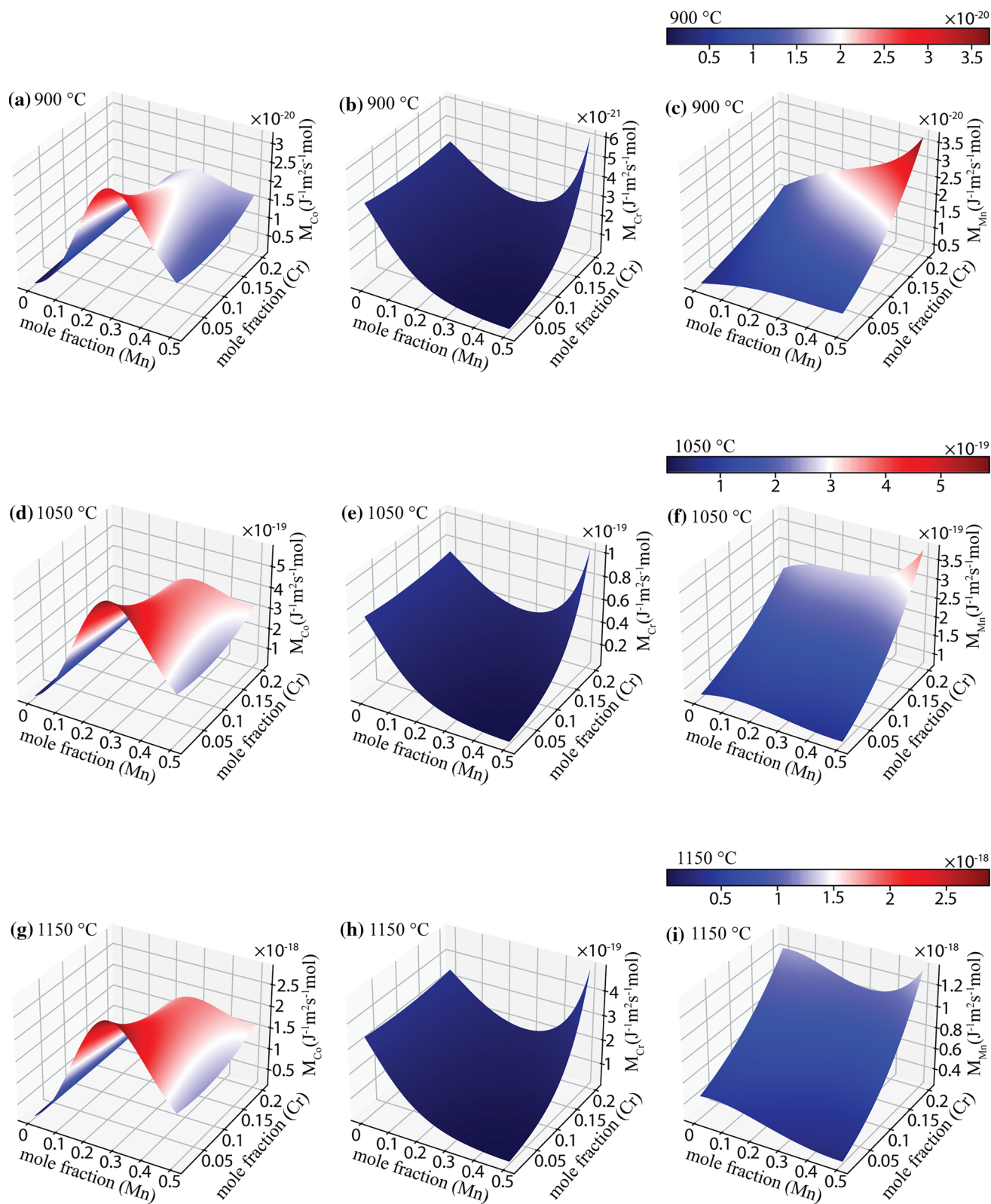


**Figure 12** Surface profiles of mobilities of Co ( $M_{Co}$ ), Cr ( $M_{Cr}$ ), and Mn ( $M_{Mn}$ ) varying with composition at **a, b, c** 900 °C, **d, e, f** 1050 °C, and **(g, h, i)** 1150 °C.

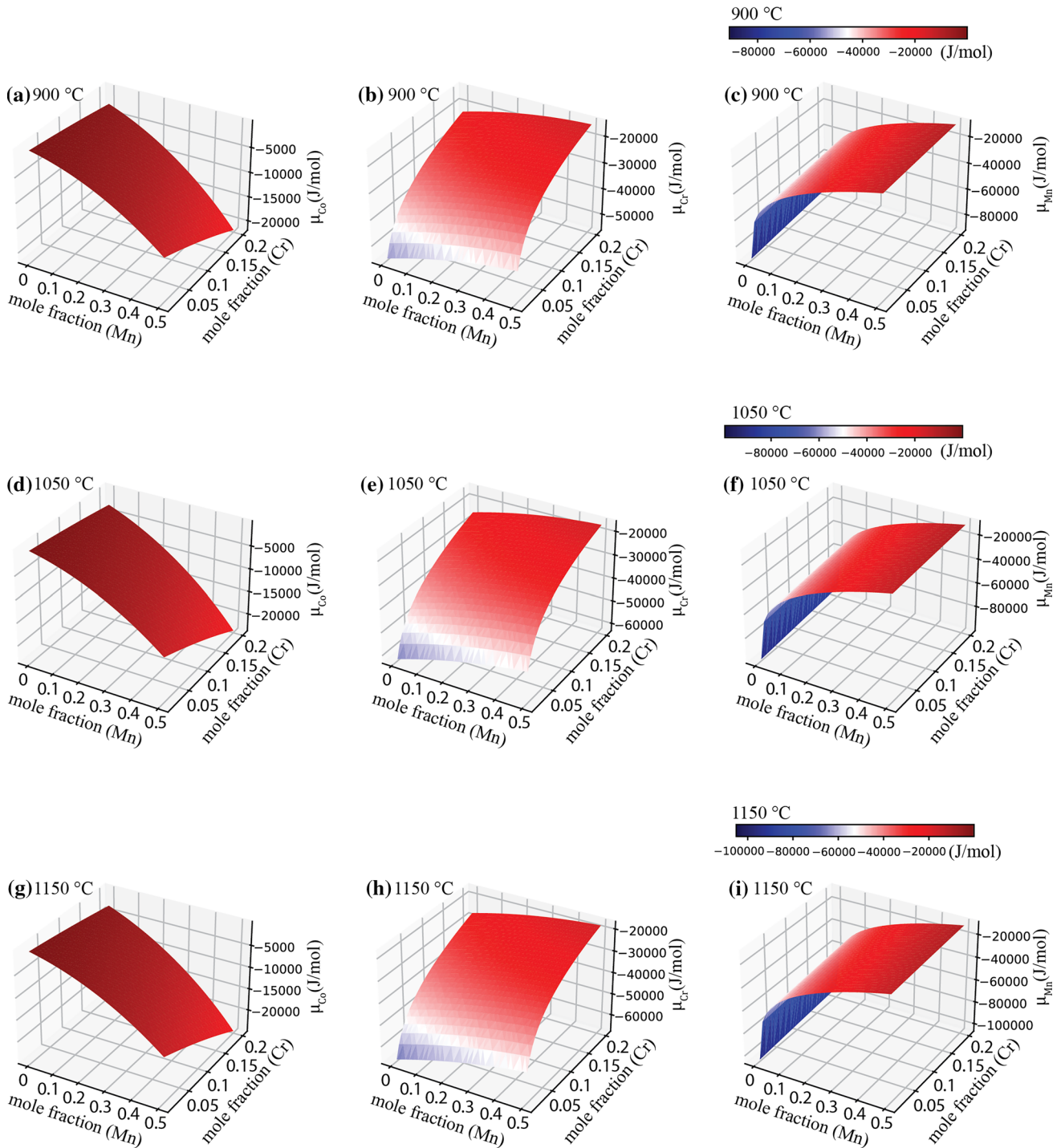


**Figure 13** Surface profiles of chemical potentials of Co ( $\mu_{Co}$ ), Cr ( $\mu_{Cr}$ ), and Mn ( $\mu_{Mn}$ ) varying with composition at **a, b, c** 900 °C, **d, e, f** 1050 °C, and **(g, h, i)** 1150 °C.

behavior of  $D_{CrCr}^{Co}$  is dependent on  $\varphi_{Mn}$ . As illustrated in Fig. 14,  $\varphi_{Mn}$  increases as Cr content rises. Hence, in high Mn region,  $D_{CrCr}^{Co}$  increases with increase in Cr content, and is dependent on mobility interaction

parameters. From Figs. 9, 10, 11,  $D_{MnMn}^{Co}$  increases and then decreases with Mn content similarly as  $\varphi_{Co}$  in Fig. 14. Hence,  $D_{MnMn}^{Co}$  depends strongly on mobility interactions between Co and Mn.  $M_{Co}$  in

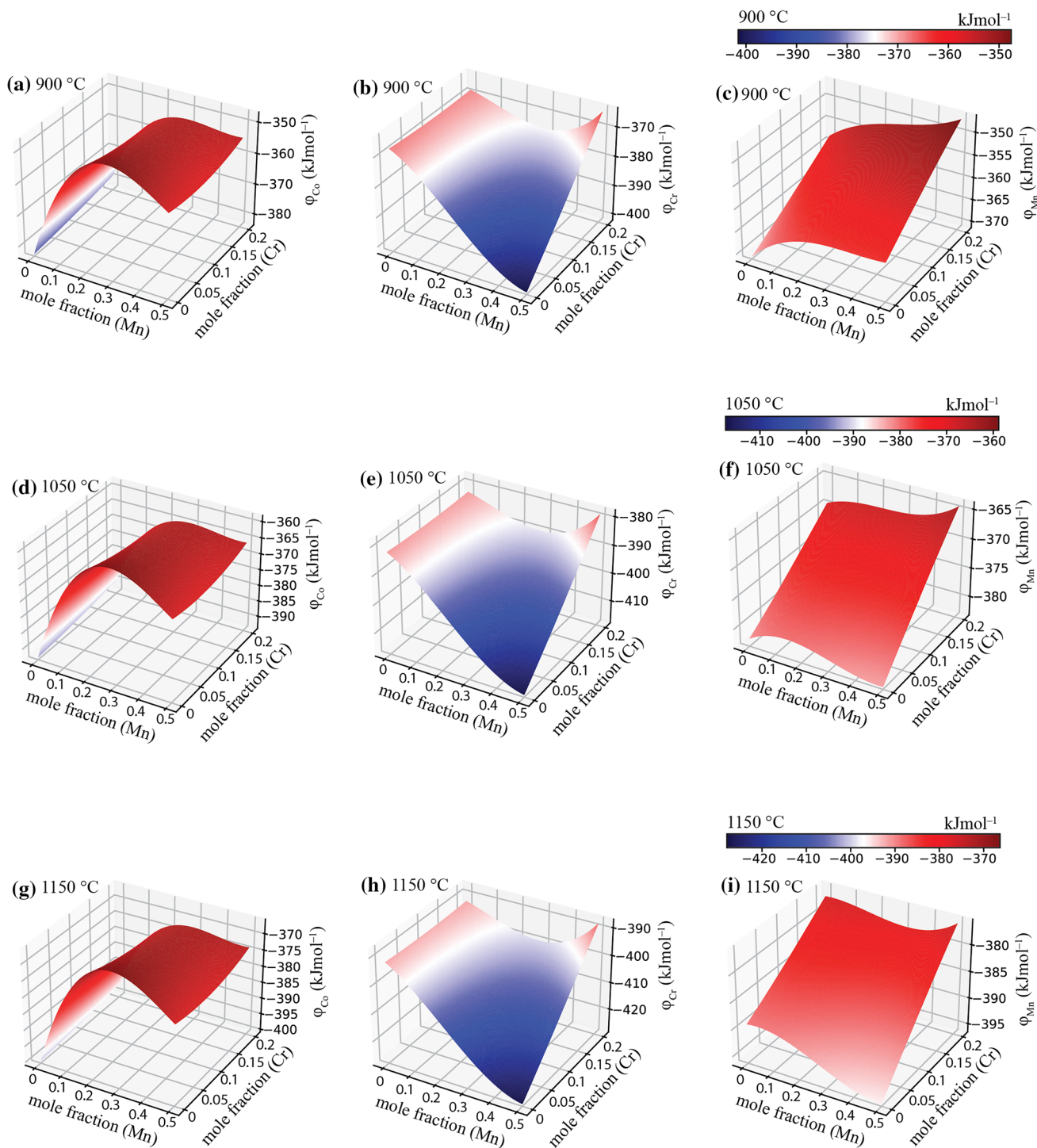


**Figure 14** Surface profiles of  $\varphi_{Co}$ ,  $\varphi_{Cr}$ , and  $\varphi_{Mn}$  varying with composition at **a, b, c** 900 °C, **d, e, f** 1050 °C, and **g, h, i** 1150 °C.

Fig. 12 is inhomogeneous across the whole composition range, and depends on only mobility interactions of Co ( $\varphi_{Co}$ ) with other elements as shown in Figs. 14a, d and g. At low Mn or otherwise high Co

content,  $M_{Cr}$  follows similar path as  $\mu_{Co}$ , and shown in Figs. 12 and 14. At high Mn content,  $M_{Cr}$  increases as  $\mu_{Cr}$  increases, and shown in Figs. 12 and 14. Hence,  $M_{Cr}$  depends both on mobility and thermodynamic

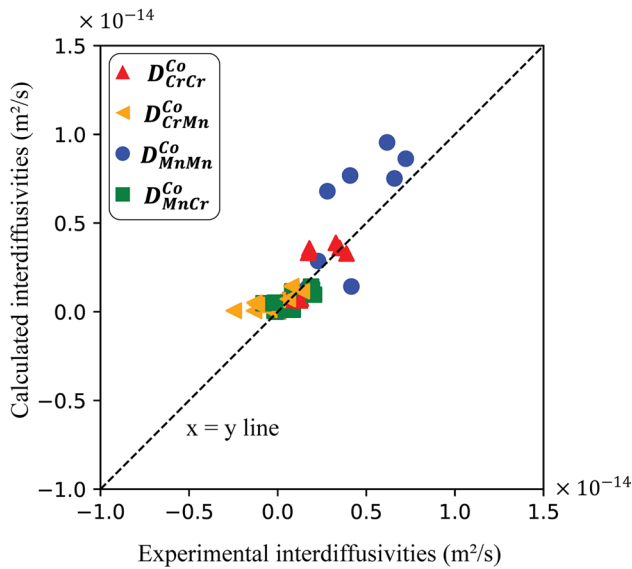


**Figure 15** Comparison of experimental ternary interdiffusivities [ $D_{CrCr}^{Co}$ ,  $D_{CrMn}^{Co}$ ,  $D_{MnMn}^{Co}$ , and  $D_{MnCr}^{Co}$ ] obtained using the Whittle–Green method at 900 °C, 1050 °C, and 1150 °C with calculated interdiffusivities.

interactions. The value range of  $\varphi_{Mn}$  is relatively narrow when compared to those of  $\varphi_{Co}$  and  $\varphi_{Cr}$ . It indicates that the diffusion mobility of Mn is more homogeneous indicating less dependency on the thermodynamic interactions, and the homogeneity increases with temperature.

Therefore, the diffusion kinetics in multicomponent alloys cannot be completely explained by the high configurational entropy effect, and thermodynamic interactions between the components of the system must also be considered. The interdiffusivities obtained from the experimental data and the Whittle–Green method were compared with those calculated using Eq. (2), as shown in Fig. 15. The deviation of experimental  $D_{CrCr}^{Co}$  values from the calculated data can be observed from Fig. 15. Considering the inherent scattering of composition profiles measured by EPMA, Eq. (20) was used to fit the experimental composition profiles in this study. The slope of the composition profile at the intersection point of two diffusion couples on the ternary isothermal section is critical for calculating the interdiffusivities accurately. Therefore, the reliability of experimental interdiffusivities of this study is restricted. As a result of this consideration, experimental interdiffusivities were not used in the

optimization process. Instead flux that can be calculated at each position across the diffusion distance of the diffusion couple was considered.

## Conclusions

A thermodynamic assessment of fcc Cr–Mn was successfully performed using the diffusion data of the Co–Cr–Mn system. The calculated phase diagram with the assessed parameters agreed with the previous experimental data. The atomic mobility parameters were determined using the assessed thermodynamic parameters and diffusion data for the Co–Cr–Mn system. The composition-dependent ternary interdiffusivities were obtained using experimental data and the Whittle–Green method. The diffusivity of Mn was higher than that of Cr in the fcc ternary Co–Cr–Mn system. The composition profiles of Co–Cr–Mn were calculated using Fick’s second law, and the ternary interdiffusivities were calculated using the mobilities. The calculated composition profiles are in excellent agreement with those obtained experimentally, thus validating the thermodynamic and kinetic assessments conducted in this study.

## Acknowledgements

This study was supported by a Grant-in-Aid for Scientific Research on Innovative Areas "High Entropy Alloys—Science of New Class of Materials Based on Elemental Multiplicity and Heterogeneity" (JSPS KAKENHI Grant Number 18H05454) and a Grant-in-Aid for Scientific Research (B) "Interfacial control of Co-based superalloy for new forging process" (JSPS KAKENHI Grant Number 18H01742). We would like to thank Editage ([www.editage.com](http://www.editage.com)) for the English language editing.

## Author contributions

SPP: Conceptualization, Methodology, Investigation, Software, Validation, Visualization, Formal analysis, Writing—Original Draft, LH: Investigation, Resources, Writing—Review & Editing, NU: Resources, Writing—Review & Editing, KO: Conceptualization, Funding acquisition, Methodology, Resources, Writing—Review & Editing, Supervision, YT: Resources,

Writing – Review & Editing, TK: Funding acquisition, Resources, Writing – Review & Editing.

## Data availability

Raw data and code will be made available on request.

## Declarations

**Conflict of interest** The authors declare that they have no known competing financial interests or personal relationships that could have appeared to influence the work reported in this paper.

**Supplementary Information** The online version contains supplementary material available at <https://doi.org/10.1007/s10853-023-08927-0>.

**Open Access** This article is licensed under a Creative Commons Attribution 4.0 International License, which permits use, sharing, adaptation, distribution and reproduction in any medium or format, as long as you give appropriate credit to the original author(s) and the source, provide a link to the Creative Commons licence, and indicate if changes were made. The images or other third party material in this article are included in the article's Creative Commons licence, unless indicated otherwise in a credit line to the material. If material is not included in the article's Creative Commons licence and your intended use is not permitted by statutory regulation or exceeds the permitted use, you will need to obtain permission directly from the copyright holder. To view a copy of this licence, visit <http://creativecommons.org/licenses/by/4.0/>.

## References

- Jensen WB (2003) The universal gas constant R. *J Chem Educ* 80:731. <https://doi.org/10.1021/ed080p731>
- Tsai MH, Yeh JW (2014) High-entropy alloys: a critical review. *Mater Res Lett* 2:107–123. <https://doi.org/10.1080/21663831.2014.912690>
- Gludovatz B, Hohenwarter A, Catoor D, Chang EH, George EP, Ritchie RO (2014) A fracture-resistant high-entropy alloy for cryogenic applications. *Science* 80(345):1153–1158. <https://doi.org/10.1126/science.1254581>
- Kaufmann K, Vecchio KS (2020) Searching for high entropy alloys: A machine learning approach. *Acta Mater* 198:178–222. <https://doi.org/10.1016/j.actamat.2020.07.065>
- Huang W, Martin P, Zhuang HL (2019) Machine-learning phase prediction of high-entropy alloys. *Acta Mater* 169:225–236. <https://doi.org/10.1016/j.actamat.2019.03.012>
- Bhandari U, Rafi MR, Zhang C, Yang S (2021) Yield strength prediction of high-entropy alloys using machine learning. *Mater Today Commun.* 26:101871. <https://doi.org/10.1016/j.mtcomm.2020.101871>
- Wang R, Zeng S, Wang X, Ni J (2019) Machine learning for hierarchical prediction of elastic properties in Fe-Cr-Al system. *Comput Mater Sci* 166:119–123. <https://doi.org/10.1016/j.commatsci.2019.04.051>
- Ruan J, Xu W, Yang T, Yu J, Yang S, Luan J, Omori T, Wang C, Kainuma R, Ishida K, Liu CT, Liu X (2020) Accelerated design of novel W-free high-strength Co-base superalloys with extremely wide  $\gamma/\gamma'$  region by machine learning and CALPHAD methods. *Acta Mater* 186:425–433. <https://doi.org/10.1016/j.actamat.2020.01.004>
- Shi R, Luo AA (2018) Applications of CALPHAD modeling and databases in advanced lightweight metallic materials. *Calphad* 62:1–17. <https://doi.org/10.1016/j.calphad.2018.04.009>
- Liu CJ, Gadelmeier C, Lu SL, Yeh JW, Yen HW, Gorsse S, Glatzel U, Yeh AC (2022) Tensile creep behavior of HfNbTaTiZr refractory high entropy alloy at elevated temperatures. *Acta Mater* 237:118188. <https://doi.org/10.1016/j.actamat.2022.118188>
- Luo H, Shi J, Wang C, Cao W, Sun X, Dong H (2011) Experimental and numerical analysis on formation of stable austenite during the intercritical annealing of 5Mn steel. *Acta Mater* 59:4002–4014. <https://doi.org/10.1016/j.actamat.2011.03.025>
- Lee B (1993) A thermodynamic evaluation of the Cr-Mn and Fe-Cr-Mn systems. *Metall Trans A* 24:1919–1933
- Ruan J, Ueshima N, Li H, Oikawa K (2021) Phase equilibria, martensitic transformations and deformation behaviors of the subsystem of Cantor alloy–low-cost Fe-Mn-Cr alloys. *Materialia* 20:101231. <https://doi.org/10.1016/j.mtla.2021.101231>
- Li H, Ruan J, Ueshima N, Oikawa K (2021) Investigation on the  $\sigma$ -phase-related equilibria in Cr-Mn-Co system. *J Alloys Compd* 867:159024. <https://doi.org/10.1016/j.jallcom.2021.159024>
- Li H, Ruan J, Ueshima N, Oikawa K (2020) Experimental investigations of fcc/bcc phase equilibria in the Cr-Mn-Ni

- ternary system. *Intermetallics* 127:106994. <https://doi.org/10.1016/j.intermet.2020.106994>
- [16] Pendem SP, Ueshima N, Oikawa K, Tsukada Y, Koyama T (2022) Thermodynamic and atomic mobility assessment of the Co–Fe–Mn system. *J Mater Sci* 57:15999–16015. <https://doi.org/10.1007/s10853-022-07612-y>
- [17] Wang P, Hu B, Huang X, Zheng C (2021) Thermodynamic assessment of the Co–Cr–Ni, Co–Cr–W and Co–Ni–W. *Calphad* 73:102252. <https://doi.org/10.1016/j.calphad.2021.102252>
- [18] Li Z, Mao H, Korzhavyi PA, Selleby M (2016) Thermodynamic re-assessment of the Co–Cr system supported by first-principles calculations. *Calphad Comput Coupling Phase Diagrams Thermochem* 52:1–7. <https://doi.org/10.1016/j.calphad.2015.10.013>
- [19] Oikawa K, Qin GW, Ikeshoji T, Kainuma R, Ishida K (2002) Direct evidence of magnetically induced phase separation in the fcc phase and thermodynamic calculations of phase equilibria of the Co–Cr system. *Acta Mater* 50:2223–2232. [https://doi.org/10.1016/S1359-6454\(01\)00433-5](https://doi.org/10.1016/S1359-6454(01)00433-5)
- [20] Houserová J, Vešál J, Friák M, Šob M (2002) Phase diagram calculation in Co–Cr system using Ab initio determined lattice instability of sigma phase. *Calphad Comput Coupling Phase Diagrams Thermochem* 26:513–522. [https://doi.org/10.1016/S0364-5916\(02\)80004-9](https://doi.org/10.1016/S0364-5916(02)80004-9)
- [21] Havrankova J, Vrestal J, Tomiska J (1998) Thermodynamics of solid Co–Cr alloys by Knudsen cell mass spectrometry and computation of the phase diagram, *Berichte Der Bunsengesellschaft Für Phys. Chemie* 102:1225–1230. <https://doi.org/10.1002/bbpc.19981020927>
- [22] Kusoffsky A, Jansson B (1997) A thermodynamic evaluation of the Co–Cr and the C–Co–Cr systems. *Calphad* 21:321–333. [https://doi.org/10.1016/S0364-5916\(97\)00033-3](https://doi.org/10.1016/S0364-5916(97)00033-3)
- [23] Wang P, Peters MC, Kattner UR, Choudhary K, Olson GB (2019) Thermodynamic analysis of the topologically close packed  $\sigma$  phase in the Co–Cr system. *Intermetallics* 105:13–20. <https://doi.org/10.1016/j.intermet.2018.11.004>
- [24] Zhao N, Liu W, Wang JJ, Lu XG, Zhang L (2020) Thermodynamic assessment of the Ni–Co–Cr system and Diffusion Study of its fcc phase, *Calphad* 71:101996. <https://doi.org/10.1016/j.calphad.2020.101996>
- [25] Shang G, Xia CH, Liu ZZ, Lu XG (2023) Thermodynamic assessment of the Co–Cr–Fe system and atomic mobility study of its fcc phase. *Calphad Comput Coupling Phase Diagrams Thermochem* 80:102526. <https://doi.org/10.1016/j.calphad.2022.102526>
- [26] Huang W (1989) An Assessment of the Co–Mn System. *Calphad* 13:231–242. [https://doi.org/10.1016/0364-5916\(89\)90003-5](https://doi.org/10.1016/0364-5916(89)90003-5)
- [27] Hellawell A, Hume-Rothery W (1957) The constitution of alloys of iron and manganese with transition elements of the first long period, *Philos. Trans R Soc London Ser. A Math Phys Sci* 249:417–459. <https://doi.org/10.1098/rsta.1957.0004>
- [28] Lugscheider E, Ettmayer P (1971) Hochtemperatur-röntgenographische Untersuchungen an manganreichen Mangan–Vanadin-und Mangan–Chrom–Legierungen. *Monatshefte Für Chemie/Chemical Mon* 102:1234–1244
- [29] Kirchner G, Uhrenius B (1974) Experimental study of the ferrite/austenite equilibrium in the Fe–Cr–Mn system and the optimization of thermodynamic parameters by means of a general mathematical method. *Acta Metall* 22:523–532. [https://doi.org/10.1016/0001-6160\(74\)90147-3](https://doi.org/10.1016/0001-6160(74)90147-3)
- [30] Han K, Sahara R, Abe T, Oikawa K, Ueshima N, Ohnuma I (2023) Phase equilibria of the Co–Cr–Mn ternary system at 700 °C. *J Alloys Compd* 965:171315. <https://doi.org/10.1016/j.jallcom.2023.171315>
- [31] Fedorov M, Wróbel JS, Chromiński W, Cieślak G, Płocińska M, Kurzydłowski KJ, Nguyen-Manh D (2023) Composition stability of single fcc phase in Cr–Fe–Mn–Ni alloys: first-principles prediction and experimental validation. *Acta Mater* 255:119047. <https://doi.org/10.1016/j.actamat.2023.119047>
- [32] Kuzovchikov S, Bajenova I, Khvan A, Cheverikin V (2023) Investigation of the hardness and enthalpy of formation of the Sigma phase and the phase equilibria in the Cr–Co–Mn system. *J Alloys Compd* 964:171263. <https://doi.org/10.1016/j.jallcom.2023.171263>
- [33] Do HS, Choi WM, Lee BJ (2022) A thermodynamic description for the Co–Cr–Fe–Mn–Ni system. *J Mater Sci* 57:1373–1389. <https://doi.org/10.1007/s10853-021-06604-8>
- [34] Zhang W, Liu D, Zhang L, Du Y, Huang BY (2014) Experimental investigation and computational study of atomic mobility in fcc ternary Co–Cr–W alloys. *Calphad Comput Coupling Phase Diagrams Thermochem* 45:118–126. <https://doi.org/10.1016/j.calphad.2013.11.005>
- [35] Borgenstam A, Engström A, Höglund L, Ågren J (2000) DICTRA, a tool for simulation of diffusional transformations in alloys. *J Phase Equilibria* 21:269–280. <https://doi.org/10.1361/105497100770340057>
- [36] Sundman B, Jansson B, Andersson J-O (1985) The Thermo–Calc databank system. *Calphad* 9:153–190. [https://doi.org/10.1016/0364-5916\(85\)90021-5](https://doi.org/10.1016/0364-5916(85)90021-5)
- [37] Weeton JW (1952) Chromium Diffusivity in Alpha Cobalt–Chromium Solid Solutions. *Trans ASM* 44:436–451

- [38] Davin LHA, Leroy V, Coutsouradis D (1963) Comparison of the diffusion of some substitution elements in nickel and cobalt. *Cobalt* 19:51–56
- [39] Green A, Whittle DP, Stringer J, Swindells N (1973) Interdiffusion in the cobalt-chromium system. *Scr Metall* 7:1079–1082. [https://doi.org/10.1016/0036-9748\(73\)90018-5](https://doi.org/10.1016/0036-9748(73)90018-5)
- [40] Liu H, Liu Y, Du Y, Min Q, Zhang J, Liu S (2019) Atomic mobilities and diffusivities in fcc Co–X (X = Mn, Pt and Re) alloys. *Calphad Comput Coupling Phase Diagrams Thermochem* 64:306–312. <https://doi.org/10.1016/j.calphad.2019.01.003>
- [41] Iijima Y, Hirano K-I, Taguchi O (1977) Diffusion of manganese in cobalt and cobalt-manganese alloys. *Philos Mag* 35:229–244. <https://doi.org/10.1080/14786437708235985>
- [42] Iijima H, Taguchi O, Hirano KI (1977) Interdiffusion in Co–Mn alloys. *Metall Trans A* 8:991–995. <https://doi.org/10.1007/BF02661584>
- [43] Zhong J, Chen W, Zhang L (2018) HitDIC: a free-accessible code for high-throughput determination of interdiffusion coefficients in single solution phase. *Calphad Comput Coupling Phase Diagrams Thermochem* 60:177–190. <https://doi.org/10.1016/j.calphad.2017.12.004>
- [44] Du C, Zheng Z, Min Q, Du Y, Liu Y, Deng P, Zhang J, Wen S, Liu D (2020) A novel approach to calculate diffusion matrix in ternary systems: Application to Ag–Mg–Mn and Cu–Ni–Sn systems. *Calphad* 68:101708. <https://doi.org/10.1016/j.calphad.2019.101708>
- [45] Chen W, Zhang L, Du Y, Tang C, Huang B (2014) A pragmatic method to determine the composition-dependent interdiffusivities in ternary systems by using a single diffusion couple. *Scr Mater* 90–91:53–56. <https://doi.org/10.1016/j.scriptamat.2014.07.016>
- [46] Esakkiraja N, Pandey K, Dash A, Paul A (2019) Pseudo-binary and pseudo-ternary diffusion couple methods for estimation of the diffusion coefficients in multicomponent systems and high entropy alloys. *Philos Mag* 99:2236–2264. <https://doi.org/10.1080/14786435.2019.1619027>
- [47] Whittle DP, Green A (1974) The measurement of diffusion coefficients in ternary systems. *Scr Metall* 8:883–884. [https://doi.org/10.1016/0036-9748\(74\)90311-1](https://doi.org/10.1016/0036-9748(74)90311-1)
- [48] Onsager L (1931) Reciprocal relations in irreversible processes. I *Phys Rev* 37:405–426. <https://doi.org/10.1103/PhysRev.37.405>
- [49] Manning JR (1970) Cross terms in the thermodynamic diffusion equations for multicomponent alloys. *Metall Mater Trans B* 1:499–505. <https://doi.org/10.1007/BF02811561>
- [50] Redlich O, Kister AT (1948) Algebraic representation of thermodynamic properties and the classification of solutions. *Ind Eng Chem* 40:345–348. <https://doi.org/10.1021/ie50458a036>
- [51] Inden G (1981) The role of magnetism in the calculation of phase diagrams. *Phys. B+C*. 103:82–100. [https://doi.org/10.1016/0378-4363\(81\)91004-4](https://doi.org/10.1016/0378-4363(81)91004-4)
- [52] Hillert M, Jarl M (1978) A model for alloying in ferromagnetic metals. *Calphad* 2:227–238. [https://doi.org/10.1016/0364-5916\(78\)90011-1](https://doi.org/10.1016/0364-5916(78)90011-1)
- [53] Virtanen P, Gommers R, Oliphant TE, Haberland M, Reddy T, Cournapeau D, Burovski E, Peterson P, Weckesser W, Bright J, van der Walt SJ, Brett M, Wilson J, Millman KJ, Mayorov N, Nelson ARJ, Jones E, Kern R, Larson E, Carey CJ, Polat İ, Feng Y, Moore EW, VanderPlas J, Laxalde D, Perktold J, Cimrman R, Henriksen I, Quintero EA, Harris CR, Archibald AM, Ribeiro AH, Pedregosa F, van Mulbregt P, Vijaykumar A, Pietro Bardelli A, Rothberg A, Hilboll A, Kloeckner A, Scopatz A, Lee A, Rokem A, Woods CN, Fulton C, Masson C, Häggström C, Fitzgerald C, Nicholson DA, Hagen DR, Pasechnik DV, Olivetti E, Martin E, Wieser E, Silva F, Lenders F, Wilhelm F, Young G, Price GA, Ingold G-L, Allen GE, Lee GR, Audren H, Probst I, Dietrich JP, Silterra J, Webber JT, Slavič J, Nothman J, Buchner J, Kulick J, Schönberger JL, de Miranda Cardoso JV, Reimer J, Harrington J, Rodríguez JLC, Nunez-Iglesias J, Kuczynski J, Tritz K, Thoma M, Newville M, Kümmerer M, Bolingbroke M, Tartre M, Pak M, Smith NJ, Nowaczyk N, Shebanov N, Pavlyk O, Brodtkorb PA, Lee P, McGibbon RT, Feldbauer R, Lewis S, Tygier S, Sievert S, Vigna S, Peterson S, More S, Pudlik T, Oshima T, Pingel TJ, Robitaille TP, Spura T, Jones TR, Cera T, Leslie T, Zito T, Krauss T, Upadhyay U, Halchenko YO, Vázquez-Baeza Y (2020) SciPy 1.0: fundamental algorithms for scientific computing in Python. *Nat Methods* 17:261–272. <https://doi.org/10.1038/s41592-019-0686-2>
- [54] Nelder JA, Mead R (1965) A Simplex Method for Function Minimization. *Comput J* 7:308–313. <https://doi.org/10.1093/comjnl/7.4.308>
- [55] Kirkaldy JS, Weichert D, Haq Z-U-H (1963) diffusion in multicomponent metallic systems: VI Some thermodynamic properties of the d matrix and the corresponding solutions of the diffusion Equations. *Can J Phys* 41:2166–2173. <https://doi.org/10.1139/p63-211>
- [56] Liu Y, Liu D, Du Y, Liu S, Kuang D, Deng P, Zhang J, Du C, Zheng Z, He X (2017) Calculated interdiffusivities resulting from different fitting functions applied to measured concentration profiles in Cu-rich fcc Cu–Ni–Sn alloys at 1073 K. *J Min Metall Sect B Metall* 53:255–262. <https://doi.org/10.2298/JMMB170626022L>

- [57] Dinsdale AT (1991) SGTE data for pure elements. *Calphad* 15:317–425. [https://doi.org/10.1016/0364-5916\(91\)90030-N](https://doi.org/10.1016/0364-5916(91)90030-N)
- [58] Fernández Guillermet A (1987) Critical evaluation of the thermodynamic properties of cobalt. *Int J Thermophys* 8:481–510. <https://doi.org/10.1007/BF00567107>
- [59] Lee BJ (1992) On the stability of Cr carbides. *Calphad* 16:121–149. [https://doi.org/10.1016/0364-5916\(92\)90002-F](https://doi.org/10.1016/0364-5916(92)90002-F)
- [60] Fernández Guillermet A, Huang W (1990) Thermodynamic analysis of manganese. *Int J Thermophys* 11:949–969. <https://doi.org/10.1007/BF00503586>
- [61] Khorasgani AR, Kundin J, Divinski SV, Steinbach I (2022) Reassessment of mobility parameters for cantor high entropy alloys through an automated procedure. *Calphad* 79:102498. <https://doi.org/10.1016/j.calphad.2022.102498>
- [62] Engström A, Ägren JÄ (1996) Assessment of Diffusional Mobilities in Face-centered Cubic Ni-Cr-Al Alloys. *Int J Mater Res* 87:92–97. <https://doi.org/10.1515/ijmr-1996-870205>
- [63] Liu Y, Zhang L, Du Y, Yu D, Liang D (2009) Atomic mobilities, uphill diffusion and proeutectic ferrite growth in Fe–Mn–C alloys. *Calphad* 33:614–623. <https://doi.org/10.1016/j.calphad.2009.07.002>
- [64] Chen J, Liu Y, Sheng G, Lei F, Kang Z (2015) Atomic mobilities, interdiffusivities and their related diffusional behaviors in fcc Co-Cr-Ni alloys. *J Alloys Compd* 621:428–433. <https://doi.org/10.1016/j.jallcom.2014.09.139>
- [65] Abrahams K, Zomorodpoosh S, Khorasgani AR, Roslyakova I, Steinbach I, Kundin J (2021) Automated assessment of a kinetic database for fcc Co-Cr-Fe-Mn-Ni high entropy alloys. *Model Simul Mater Sci Eng.* 29:055007. <https://doi.org/10.1088/1361-651X/abf62b>
- [66] Liu D, Zhang L, Du Y, Xu H, Jin Z (2013) Ternary diffusion in Cu-rich fcc Cu-Al-Si alloys at 1073 K. *J Alloys Compd* 566:156–163. <https://doi.org/10.1016/j.jallcom.2013.03.024>

**Publisher's Note** Springer Nature remains neutral with regard to jurisdictional claims in published maps and institutional affiliations.